An Image-Based Model of Calcium Waves in Differentiated Neuroblastoma Cells

Charles C. Fink,* Boris Slepchenko,[†] Ion I. Moraru,[‡] James Watras,[§] James C. Schaff,[†] and Leslie M. Loew[*†]

*Department of Physiology, [†]Center for Biomedical Imaging Technology, [‡]Department of Surgery, and [§]Department of Medicine, University of Connecticut Health Center, Farmington, Connecticut 06030 USA

ABSTRACT   Calcium waves produced by bradykinin-induced inositol-1,4,5-trisphosphate (InsP$_3$)-mediated release from endoplasmic reticulum (ER) have been imaged in N1E-115 neuroblastoma cells. A model of this process was built using the "virtual cell," a general computational system for integrating experimental image, biochemical, and electrophysiological data. The model geometry was based on a cell for which the calcium wave had been experimentally recorded. The distributions of the relevant cellular components [InsP$_3$ receptor (InsP$_3$R)], sarcoplasmic/endoplasmic reticulum calcium ATPase (SERCA) pumps, bradykinin receptors, and ER] were based on 3D confocal immunofluorescence images. Wherever possible, known biochemical and electrophysiological data were used to constrain the model. The simulation closely matched the spatial and temporal characteristics of the experimental calcium wave. Predictions on different patterns of calcium signals after InsP$_3$ uncaging or for different cell geometries were confirmed experimentally, thus helping to validate the model. Models in which the spatial distributions of key components are altered suggest that initiation of the wave in the center of the neurite derives from an interplay of soma-biased ER distribution and InsP$_3$ generation biased toward the neurite. Simulations demonstrate that mobile buffers (like the indicator fura-2) significantly delay initiation and lower the amplitude of the wave. Analysis of the role played by calcium diffusion indicated that the speed of the wave is only slightly dependent on the ability of calcium to diffuse to and activate neighboring InsP$_3$ receptor sites.

INTRODUCTION

A cell biological process is composed of many individual interacting biochemical components that are spatially organized within membranes, organelles, and cytoplasm. A prerequisite for an understanding of the process is, therefore, data identifying all of these molecules, the kinetics of their reactions, and their topological organization within the cell. Modern techniques are making it possible to acquire all this information for many cell biological phenomena, and a large mass of data is accumulating. However, as has been incisively described by Dennis Bray (Bray, 1997), a thorough knowledge of the components still begs questions of how all the biochemistry is coordinated to deliver the cellular behavior: can we develop a quantitative or even qualitative understanding of the behavior based on the complex spatial and temporal interplay of its components? Are all of the identified components sufficient and necessary? How sensitive is the overall process to perturbations of a given component? A second prerequisite, therefore, is that all these data be gathered and integrated with the appropriate physical/chemical laws to permit creation of a dynamic visual model of the biology.

Intracellular calcium dynamics may be a particularly feasible target for attempts to build such models because of the many experimental tools available to study both the molecular components underlying intracellular calcium release and the calcium release events themselves. Also, the physical/chemical laws can be readily expressed in terms of differential equations describing reaction kinetics, fluxes through membranes, and diffusion. Indeed, calcium waves and oscillations have been the subjects of many theoretical treatments that have provided important mathematical and physical insights (De Young and Keizer, 1992; Keizer and De Young, 1992; Atri et al., 1993; Li and Rinzel, 1994; Tang and Othmer, 1994; Jafri, 1995; Roth et al., 1995; Sneyd et al., 1995; Keizer and Levine, 1996; Kupferman et al., 1996, 1997). To achieve such insights and reasonable computation times, these treatments strive for ways to reduce the complexity of the system; particular emphasis is placed on techniques for avoiding or simplifying partial differential equations in formulating the spatial component of the problem. These efforts can lead to elegant levels of abstraction that may offer broadly applicable generalizations. However, such models can become disconnected from the experiments that may have originally prompted their development.

We have developed a comprehensive image-based model of a bradykinin (BK)-induced intracellular calcium wave in differentiated N1E-115 neuroblastoma cells. A key conclusion from this analysis is that the neuronal morphology plays a key role in controlling and shaping the inositol-1,4,5-trisphosphate (InsP$_3$) dynamics that underlies the calcium wave. This is the subject of a brief report (Fink et al., 1999b). In the present paper we provide a thorough description of the elements comprising the model and a wide-ranging exploration of its predictions. Our aim was to sys-

tematically collect relevant experimental data to maximize constraints within the model. Much of this data comes from our own experiments, but we relied on the extensive literature related to this system as well. The model was assembled within a unique computational system, the "virtual cell" (VC) (Schaff et al., 1997), that permits the construction of models from experimental biochemical, electrophysiological, and image data and solves the partial differential equations for the system numerically. The model was mapped to an image of a cell from which a calcium wave was captured by microscope imaging of a fluorescent calcium indicator. The simulation resulting from this model was a near-quantitative match to the experimentally observed calcium wave. An advantage of simulation is that biological processes that can't be imaged experimentally (such as $[InsP_3]_{cyt}$) can be visualized. Additionally, physiological conditions that are difficult to manipulate experimentally (such as varied geometry, ER distribution, buffering, and diffusion coefficients) can be investigated via computer simulation. The strength of the model is probed by running simulations that can be tested experimentally, and by examining cells of varying morphology. Beyond the application to calcium dynamics, this approach may serve as a paradigm for processing the vast amounts of data that are being gathered on the mechanisms of cell biological processes.

MATERIALS AND METHODS

Cell culture

N1E-115 neuroblastoma (Nb) cells (obtained from Dr. Marshall Nirenberg, NIH) were grown and maintained in DMEM containing 10% fetal bovine serum (FBS) and 1% antimitotics/antimycotics, and kept in a 5% CO_2 incubator at 37°C. Cells were grown until 50% confluent before plating on individual coverslips. Differentiation was induced by changing the medium to DMEM plus 0.5% FBS, 1% antimitotics/antimycotics, and 1% DMSO, which was morphologically complete 60–72 h later. Coverslips were kept in EBSS and mounted on an open-welled plastic chamber that was placed on the microscope stage.

Calcium imaging

N1E-115 Nbs were cooled to 10°C for 10 min (to prevent dye internalization into organelles) before staining with fura-2/AM (5 μM) and 0.25% Pluronic-127 for 30–60 min at room temperature, followed by a 30-min recovery in EBSS at 37°C. Images were acquired using a high-speed Photometrics CCD camera (frame transfer EEV37 chip) on an inverted Zeiss microscope, controlled by Inovision software on a Silicon Graphics workstation. Coverslips were mounted on an open-welled chamber. The cells were bathed in pH-controlled EBSS and maintained at 37°C. Ratio pairs of 340- and 380-nm excitation were collected for some experiments, with emission passed through a rhodamine filter. Using this acquisition protocol, ratio pairs could be collected approximately once a second. Because the BK-induced calcium waves are typically very fast, faster imaging was necessary to resolve the geometry of the calcium wave propagation. Faster imaging was possible using only the 380-nm excitation wavelength, in which images could be obtained every 65 ms. Cell exposure during excitation was kept to a minimum by using 4×4 binning (resulting

in 128×128 images) and increased gain settings, but always maintaining at least a 5-to-1 cell-to-background intensity ratio. BK was added in 20-μl aliquots to the cell chamber, so that the exposure was nearly instantaneous but with as little cellular disturbance as possible.

Calcium analysis

Daily calibrations were performed to obtain values for R_{min}, R_{max}, and B_{max}, with K_D defined as 224 nM. Using formulas defined by Grynkiewicz et al. (1985), ratio values were converted to calcium concentrations. To estimate calcium values for the single wavelength experiments, the following equation was used: $[Calcium] = K_D [(F - F_{min})/(F_{max} - F)]$. All image analysis was done on Silicon Graphics workstations using the Inovision Corp. (Raleigh, NC) programs Ratiotool, used for calcium analysis of dual wavelength experiments, and ISee, on which graphical analysis programs were constructed to do the single wavelength analysis. Wave velocity is calculated by taking the wavefront at any given time to be the position corresponding to 50% of the free cytosolic calcium ($[Ca^{2+}]_{cyt}$) peak.

InsP$_3$ uncaging

Cells were microinjected with a solution containing 1–10 mM 1-(2-nitrophenyl)ethyl (NPE)-InsP$_3$ (Calbiochem, La Jolla, CA) and 0.67 mM Calcium Green-1 (CG-1)/10 kD Dextran (Molecular Probes, Eugene, OR) in a solution containing 135 mM potassium, 10 mM aspartate, 10 mM HEPES, buffered to 7.2. Cells were imaged on the Zeiss (Thornwood, NY) LSM410 confocal microscope after a 30-min recovery period. All experiments on the confocal microscope were performed at room temperature (22–24°C) (ratio imaging experiments with the CCD camera-based system showed that there were no significant differences between BK-induced calcium waves at 22°C versus 37°C). A z-section through the soma was taken to quantify the concentration of CG-1; thus, the dilution of NPE-InsP$_3$ that has occurred with injection can also be calculated (Fink et al., 1998, 1999a). A z-slice was selected so that both the neurite and soma were in focus, and initial CG-1 fluorescence was scanned at 488 nm with a 515–560-nm emission. For uncaging, the cell was scanned with 364-nm laser light followed immediately by a time series of CG-1 fluorescence at 1-s intervals. After the experiment, calcium calibration slides of CG-1 were scanned at the same settings as had been used for the cell. Calcium analysis was then performed as described above for single wavelengths.

Electron microscopy

Cells were fixed in 2.5% glutaraldehyde in 0.1 M sodium cacodylate buffer, postfixed in 1% osmium tetroxide–0.8% potassium ferracyanide in 0.1 M sodium cacodylate buffer, and stained with 1% aqueous uranyl acetate. Cells were then embedded in PolyBed resin, thin-sectioned, and visualized on a JEOL 100 CX electron microscope.

Immunolocalization

Differentiated N1E-115 Nb cells (preparation described in the Cell Culture section) were fixed by a 10-min incubation at room temperature in a 4% paraformaldehyde/0.1% glutaraldehyde solution. After washing with phosphate-buffered saline (PBS), fixed cells were then permeabilized in 0.01–0.1% Triton-X/PBS solution for 2–5 min at room temperature, followed by 2 h of nonspecific blocking in a 5% milk/PBS solution. After washing, the cells were incubated with the primary antibody (in a 3% bovine serum albumin (BSA)/PBS solution) for up to 19 h at 4°C. Primary antibodies used were rabbit anti-IP$_3$I-receptor (1:100 dilution; generously donated by Barbara Ehlich), mouse anti-IP$_3$II-receptor (1:50 dilution; Calbiochem), mouse anti-IP$_3$III-receptor (1:100 dilution; Tranduction Laboratories, Lex-

ington, KY), rabbit anti-BK2-receptor (1:50 dilution; generously donated by Werner Esterl-Muller), rabbit anti-BIP (1:100; StressGen), and rabbit anti-SERCA2 (1:10 dilution; generously donated by Sergei Syrbu). For the negative controls, either the primary antibody was omitted or the primary was substituted with IgG of the appropriate animal. After the wash, the cells were incubated with the secondary antibody (goat anti-mouse or anti-rabbit rhodamine, 1:100 dilution, Molecular Probes) in 3% BSA/PBS for 1 h at room temperature. For BK imaging, 1:50 goat anti-rabbit Liss-Rhodamine (Jackson Pharmaceuticals) was used as the secondary antibody.

After a final wash, the coverslips were mounted on glass slides in a glycerol/PBS anti-fade solution (Molecular Probes) and sealed with nail polish. Cells were then visualized with the confocal microscope using a 568-nm excitation laser line with emission collected over 630 nm. 3D section analysis was done using VoxelView (Vital Images, Minneapolis, MN) software package on Silicon Graphics workstations.

Endoplasmic reticulum imaging in living cells

To image endoplasmic reticulum (ER) distribution in living cells we labeled the ER membrane by microinjection of a solution of lipophilic dye in oil. Di-18:2:ANNEPS (supplied by Joseph P. Wuskell in this laboratory, but also available from Molecular Probes, Inc., Eugene, OR) was dissolved in soybean oil, back-filled into a glass pipette, and microinjected into the cell by pressure ejection, similar to the ER-staining technique established by Terasaki (Terasaki and Jaffe, 1991) with Di-I in *Xenopus* oocytes. The dye-saturated oil droplet is positioned in the cytoplasm so that it contacts the ER, but not the plasma membrane. Over the next 30 min the highly lipophilic dye gradually diffuses along the ER membranes, eventually staining a membranous structure that can be morphologically identified as primarily ER. Images were acquired on a Zeiss confocal microscope using a 488-nm excitation laser line with emission collected over 590 nm. Three-dimensional section analysis was done using the VoxelView software package on Silicon Graphics workstations. An example of an Nb cell imaged in this way can be seen in Fig. 2a.

[InsP₃] determination

Cells were grown to near-confluency in 12 culture dishes of 500 cm² each and then induced to differentiate by the standard procedure. Cells on ice were mechanically removed from the dishes with plastic cards. Suspended cells were washed 3 times with EBSS and concentrated into a final volume of 3 ml; protein concentration determined by a Lowry assay was 57 mg/ml. After addition of 500 nM BK, 100-μl aliquots of the cells were quenched at specific times by addition of 50 μl 12% perchloric acid. A control aliquot of cells was loaded with fura-2-AM and examined under the fluorescence microscope to check that the cells had normal responsiveness to BK. InsP₃ mass was calculated using a competitive radioligand binding assay with canine cerebellar microsomes, 10 nM ³H-InsP₃, and various concentrations of nonradioactive InsP₃ as described by Benevolensky et al. (1994). Effects of inhibitors were calculated by Scatchard analysis. Intracellular volume measurements were performed by determining excluded volumes with ³H-inulin (Amersham Pharmacia Biotech, Inc., Piscataway, NJ) relative to total volume determined with ¹⁴C-urea. Briefly, known concentrations of ³H-inulin and ¹⁴C-urea are added to an aliquot of cells in a known volume. After centrifugation, the relative dilutions, determined by scintillation counting, of inulin (which is excluded from the intracellular volume) and urea (which rapidly equilibrates with the intracellular volume) provide a measure of the fraction of the initial volume taken up by the cytoplasm. This, divided by the cell count, yields the intracellular volume.

A model for 2D simulations of calcium waves in neuroblastoma cells

Calcium waves in differentiated N1E-115 Nb cells, experimentally initiated by applying BK, are the result of calcium release from the ER through channels activated by InsP₃. InsP₃, in turn, is released from the plasma membrane under the stimulus effect and diffuses throughout the cell. The mathematical formulation of the calcium and InsP₃ dynamics incorporates the models of the major components participating in the phenomenon: ER, InsP₃ receptors (InsP₃R), and sarcoplasmic/endoplasmic reticulum calcium ATPase (SERCA) pumps embedded in the ER membrane, plasma membrane extrusion mechanisms, and calcium buffering in the cytosol. In the Appendix we describe all the components in detail. To combine them into a comprehensive model we use a new, redesigned, and rigorously tested version of the VC, a general framework for image-based modeling of cell biological processes (Schaff et al., 1997). See the Appendix for detailed equations and parameters used for modeling.

RESULTS

BK-induced calcium dynamics in differentiated N1E-115 Nb cells

When 500 nM BK, a saturating concentration, is applied to a differentiated N1E-115 Nb cell, a nonoscillatory calcium wave is initiated with dynamics and geometry that are highly reproducible from cell to cell. Responses were seen in 79/93 of the cells observed; specifically, the calcium increase is typically seen to initiate in the middle of a neurite after a short latency (2.97 ± 0.93 s; $n = 16$), rapidly propagating in both directions to fill both the soma and the distal neurite. Wave propagation was faster in the neurite than the soma (147.8 ± 93.9 μm/s vs. 39.2 ± 14.9 μm/s, $n = 16$; $p < 0.001$, ANOVA). The initial level of calcium is ~50 nM and rises to a peak of 1000 nM. After the spread of the calcium wave, decay of the $[Ca^{2+}]_{cyt}$ occurs first at the site where the wave initiated with the more distal areas recovering at a slightly later time point, but with similar recovery kinetics. A representative example is shown in Fig. 1.

The events underlying this calcium wave have been studied in a number of laboratories (Snider and Richelson, 1984; Ueda et al., 1986; Higashida and Brown, 1987; Glanville et al., 1989; Farooqui et al., 1990; Monck et al., 1990; Iredale et al., 1992; Coggan and Thompson, 1995, 1997). These studies provide a wealth of information from which a comprehensive model can be initiated. The following events take place:

1. Binding of BK to its receptor initiates a G-protein cascade, activation of phospholipase C, and breakdown of phosphatidylinositol bisphosphate (PIP₂) to InsP₃;
2. InsP₃ diffuses from the plasma membrane to the ER, where it activates calcium release through the InsP₃R channel;
3. The released calcium raises the level of $[Ca^{2+}]_{cyt}$ but also binds to fixed and mobile calcium buffers;
4. $[Ca^{2+}]_{cyt}$ is pumped back into the endoplasmic reticulum through the SERCA.
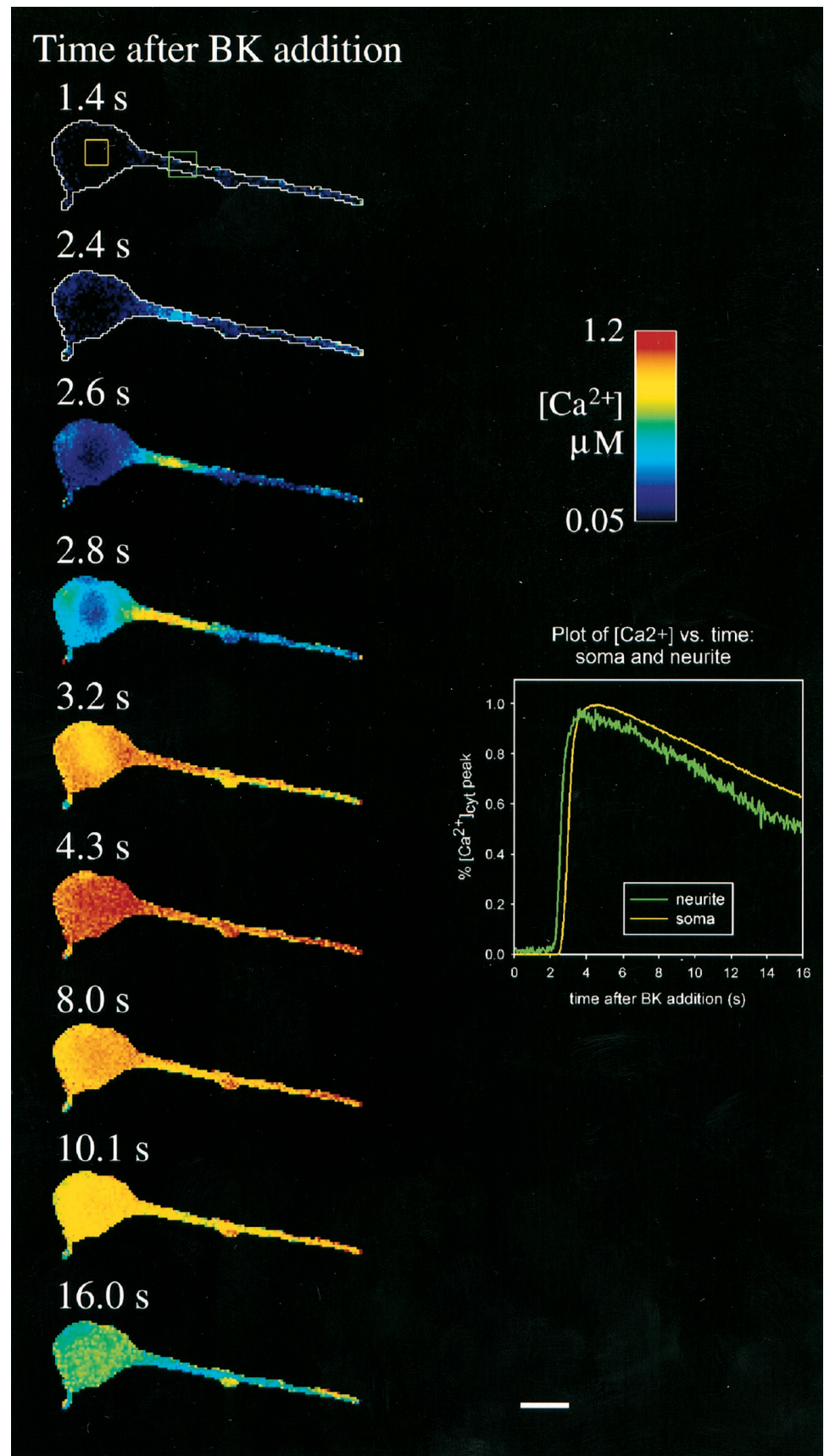
FIGURE 1 BK-induced calcium wave in an N1E-115 Nb cell. BK (500 nM) was externally applied to the bathing medium of a cell stained with fura-2. Fluorescence from the 380-nm excitation was collected with a cooled CCD camera, converted to $[Ca^{2+}]$, and displayed in pseudocolored form. For regions of interest in the soma and neurite (indicated by the colored rectangles), the relative change in $[Ca^{2+}]$ versus time was plotted in the lower right-hand corner. Scale bar = 25 μM.

Simulations are facilitated by the absence of other possible mechanisms for calcium signaling, such as calcium-induced calcium release via the ryanodine receptor and calcium entry through plasma membrane channels (Iredale et al., 1992; Wang and Thompson, 1995). However, for events 1–4, all the kinetic details and the spatial distributions and levels of all the relevant molecular species will have to be considered to construct a VC model of the calcium wave.

Model components

The cell shown in Fig. 1 was used to define the simulation geometry. The growth cone at the tip of the neurite was outside the field of view in the calcium images of Fig. 1, but was included in the simulation geometry. Cytosol, extracellular milieu, and nucleus were defined based on intensity thresholds and interactive segmentation. Although no specific nuclear marker was used in this cell, the nuclear location and geometry could be estimated from the calcium indicator images. Membranes are defined as being the border between these cellular structures. Because of the intricate reticular structure, the ER was modeled as a continuous network of varying density in the cytosol. It was apparent from electron microscopy that the ER density in the soma was greater than the ER density in the neurite, as exemplified in Fig. 2 *a*. Fig. 2 *b* shows that this variation in ER density can be visualized in a living cell by using the oil droplet staining technique developed by Mark Terasaki (Terasaki and Jaffe, 1991, and see Methods section).

However, to build our model, we needed to image not only the ER distribution itself, but also the distribution of InsP$_3$R and SERCA in the ER membrane. The distribution of the bradykinin receptor (BKR) along the plasma membrane is another obvious piece of information required for the model. To collect this data required analysis of immunofluorescently stained fixed cells. Western blot and ratiometric PCR analysis (data not shown) indicated that the type 1 InsP$_3$R isoform (InsP$_3$1-R) was dominant. Immunofluorescent labeling in fixed N1E-115 Nb cells was carried out for BKR, InsP$_3$1-R, SERCA2, and BIP (an ER-resident heat shock protein used as a generic ER marker). A 3D volume rendering of the SERCA distribution is shown as an example in Fig. 3 *a*. Three-dimensional images were analyzed to calculate the fluorescence intensities in central sections from six regions of each cell: distal soma, proximal soma, proximal neurite, middle neurite, distal neurite, and growth cone. These data were then corrected for the relative blurring occurring in the different regions of the cell by making estimates using convolutions of primitive analytical volumetric solids, chosen to best-approximate the cellular geometry, with the confocal microscope point spread function (Fink et al., 1998). The mean corrected relative intensities for all cells analyzed (~20 cells for each immunostain) were then mapped onto the cellular geometry used for simulations as shown in Fig. 3 *b*; InsP$_3$1-R, SERCA2, and

BIP had statistically indistinguishable cellular distributions ($p < 0.05$), indicating that SERCA and InsP$_3$R are evenly distributed along the ER membrane. Thus, only the ER distribution is displayed in Fig. 3 *b*, as the relative SERCA and InsP$_3$R distributions are taken as identical. Table 1 details the average distributions of the SERCA, InsP$_3$R, and BIP, collected under the columns labeled ER, and the distribution of the bradykinin receptor, labeled BKR, together with the respective standard errors (SE) and standard deviations (SD), for the six regions of the cell illustrated in Fig. 3 *b*. For some simulations the modeled distributions were allowed to deviate from these average values, but never more than one standard deviation. This was done to reflect the heterogeneity of the population and to obtain a "best fit" for a particular experiment when compared to its respective simulation.

Concentrations of exogenous buffers (fura-2 and CG-1) were determined by a method described in detail in a previous publication (Fink et al., 1998). [Fura-2]$_{cyt}$ and [CG-1]$_{cyt}$ were estimated to be 75 μM and 18 μM, respectively.

The time course of [InsP$_3$]$_{cyt}$ was constrained by experimental measurements using competitive radioligand binding. Differentiated Nb cells were put into suspension, which facilitated cellular volume calculations with ^{3}H-inulin and ^{14}C-urea. Control experiments were performed showing that Nbs in suspension exhibit calcium responses to BK, as seen in differentiated cells grown on glass coverslips (data not shown). The results of these experiments are superimposed on the [InsP$_3$]$_{cyt}$ versus time graph in Fig. 4. These measurements do not finely resolve dynamic [InsP$_3$]$_{cyt}$, and represent the mean for the entire cellular volume in suspension. The values for [InsP$_3$]$_{cyt}$ determined by this method are consistent with results of quantitative InsP$_3$ uncaging experiments (Fink et al., 1999b).

Parameters that were not directly measured in our laboratory were obtained from the literature. Where this was not available, parameters were estimated within reasonable physical constraints (e.g., diffusion reaction coefficients from molecular weights and viscosities, and on-rates no faster than the diffusion limit). These parameters include solute diffusion coefficients (InsP$_3$, calcium, fura-2, CG-1), InsP$_3$1-R, SERCA2, and plasma membrane calcium extrusion pump kinetics, [Ca^{2+}]$_{ER}$, and the concentration and dissociation constants for endogenous immobile calcium buffers. All the values and their origins are provided in Tables 2–4 in the Appendix.

Simulated BK-induced calcium waves

The results for the simulation of a BK-induced calcium wave in N1E-115 Nb cells are shown in Fig. 4. For this simulation, distributions of BKR and ER (along with InsP$_3$-R and SERCA2) are the average values for various regions of the cell (as shown in Fig. 3 *b*). The calcium dynamics closely follows that observed in the real cell (Fig.
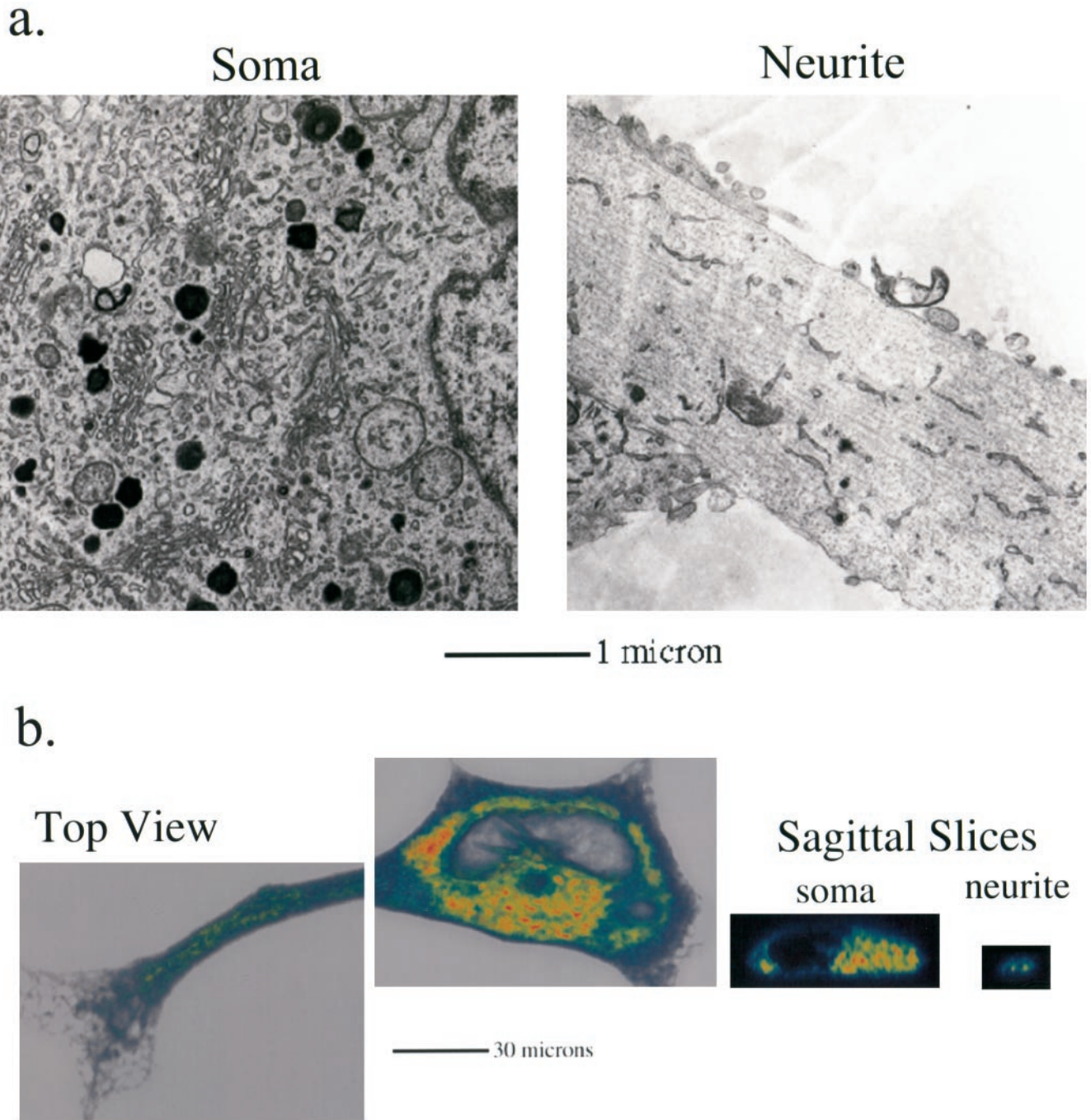
a.

Soma

Neurite

———— 1 micron

b.

Top View

Sagittal Slices
soma   neurite

———— 30 microns

FIGURE 2   The ER is more abundant in the soma than the neurite. (*a*) Electron micrographs of ER in the soma and neurite of N1E-115 neuroblastoma cells. (*b*) The ER of a live cell is visualized with a fluorescent lipophilic dye, di-18:2-ANEPPS. The cell was microinjected with Di-18:2-ANEPPS dissolved in mineral oil, such that the ER is fluorescently labeled several minutes subsequent to injection. Z-sections were collected on a confocal microscope for 3D reconstruction and analysis. A top view of a pseudocolored 3D reconstruction is shown, with sagittal slices through the soma and neurite to the right.

1) on which this simulation geometry is based. In addition to $[Ca^{2+}]_{cyt}$, simulation results can be displayed for experimentally inaccessible components and variables, such as $[InsP_3]_{cyt}$ and the P_O (open probability) of the $InsP_3$-R. The time course of $[InsP_3]$ for the whole cell was experimentally determined using competitive radioligand binding tech-niques. The data points from these experiments, shown in blue in the plot, closely follow the simulated $[InsP_3]$ in the soma. Because the soma accounts for most of the cell volume, the $[InsP_3]$ there is just a small underestimate of the $[InsP_3]$ integrated over the whole cell. This correspondence gives us confidence in the simulated $[InsP_3]$ time course.
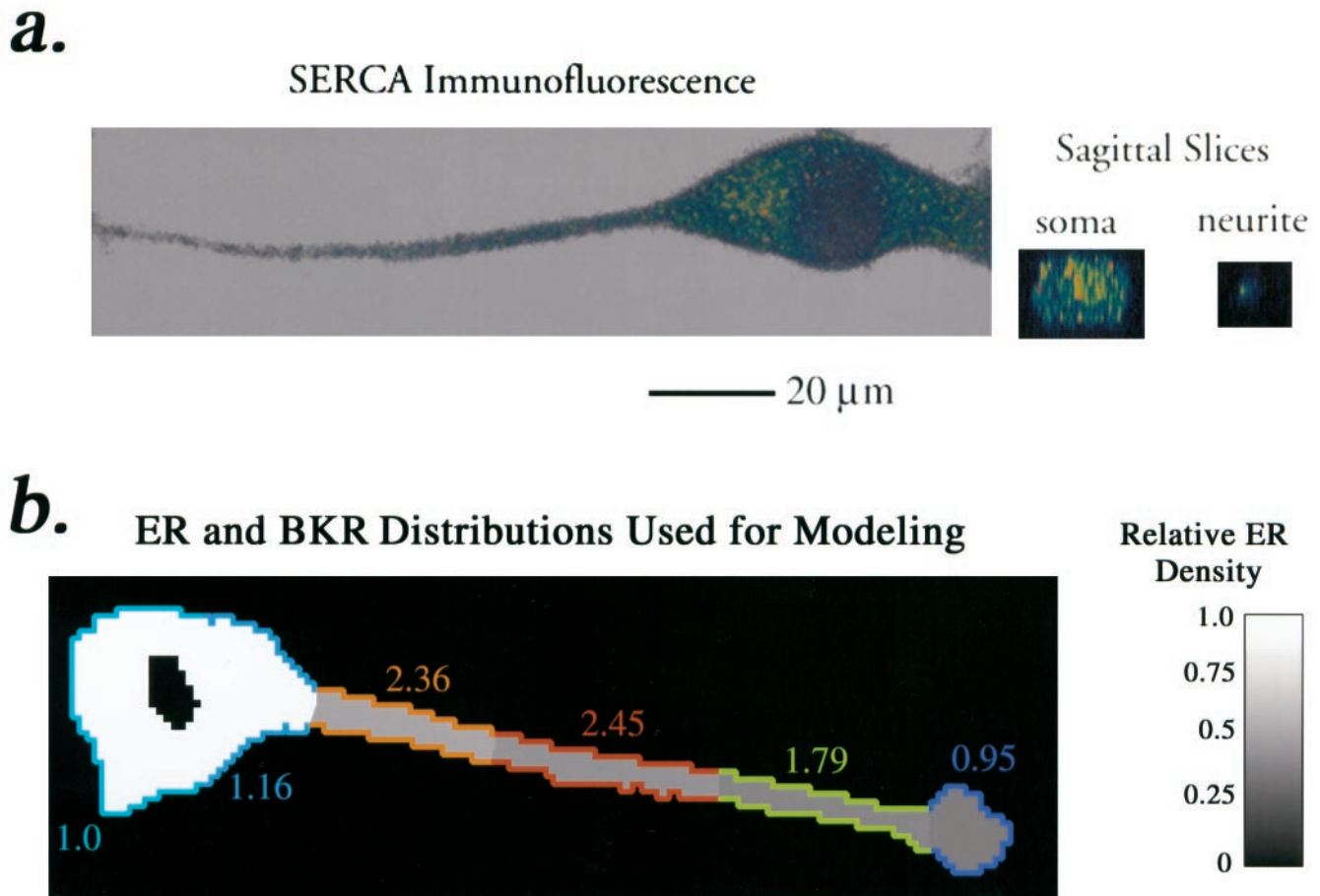
FIGURE 3 (*a*) Example of a 3D immunofluorescence image used to determine intracellular distributions. In this example, an N1E-115 Nb cell has been fixed and stained with an antibody to SERCA2. (*b*) Intracellular distributions of BKR and ER/InsP₃-R/SERCA2, projected onto the morphology of the cell in Fig. 1. The relative BKR surface densities along the plasma membrane for the six averaged regions of the cell are shown in color-coding along the periphery; the average distribution of the ER is identical to that of InsP₃R and SERCA, and is shown as gradations of gray values within the cell with a scale indicator on the right. In both cases the densities are expressed relative to the leftmost section of the soma taken as unity.

The sequence of key events in the simulation results are as follows: 1) rapid build-up of $[InsP_3]$ in the neurite with much lower amplitudes following rapidly in the soma and distal neurite; 2) newly produced $InsP_3$ and basal calcium cooperatively open the $InsP_3$-R in a relatively tight bidirectional wave; 3) calcium release from the ER, initiating in the neurite and propagating through the entire cell with an approximately uniform maximal amplitude of 1.2 μM; 4) elevated $[Ca^{2+}]_{cyt}$ closes the $InsP_3$-R; 5) basal $[InsP_3]_{cyt}$ is restored by $InsP_3$ degradation; and 6) basal $[Ca^{2+}]_{cyt}$ is restored by SERCA-mediated refilling of the ER stores and calcium extrusion via plasma membrane pumps. The fact that both the $InsP_3$ amplitude and the P_O for the $InsP_3$-R calcium channel attain much higher values in the neurite than in the soma, while the amplitude of the resultant $[Ca^{2+}]_{cyt}$ signal reaches approximately equal values throughout the cell is noteworthy and will be addressed in the Discussion.

Inasmuch as the simulation in Fig. 4 was based on the average values for the distributions of receptors and pumps rather than the values that might pertain to the specific cell examined in our experiment (Fig. 1), the simulation and experimental results are close but do not precisely match. However, by slightly modifying the intracellular distributions within a standard deviation of the mean it was possible

TABLE 1   Relative distributions of ER and bradykinin receptor

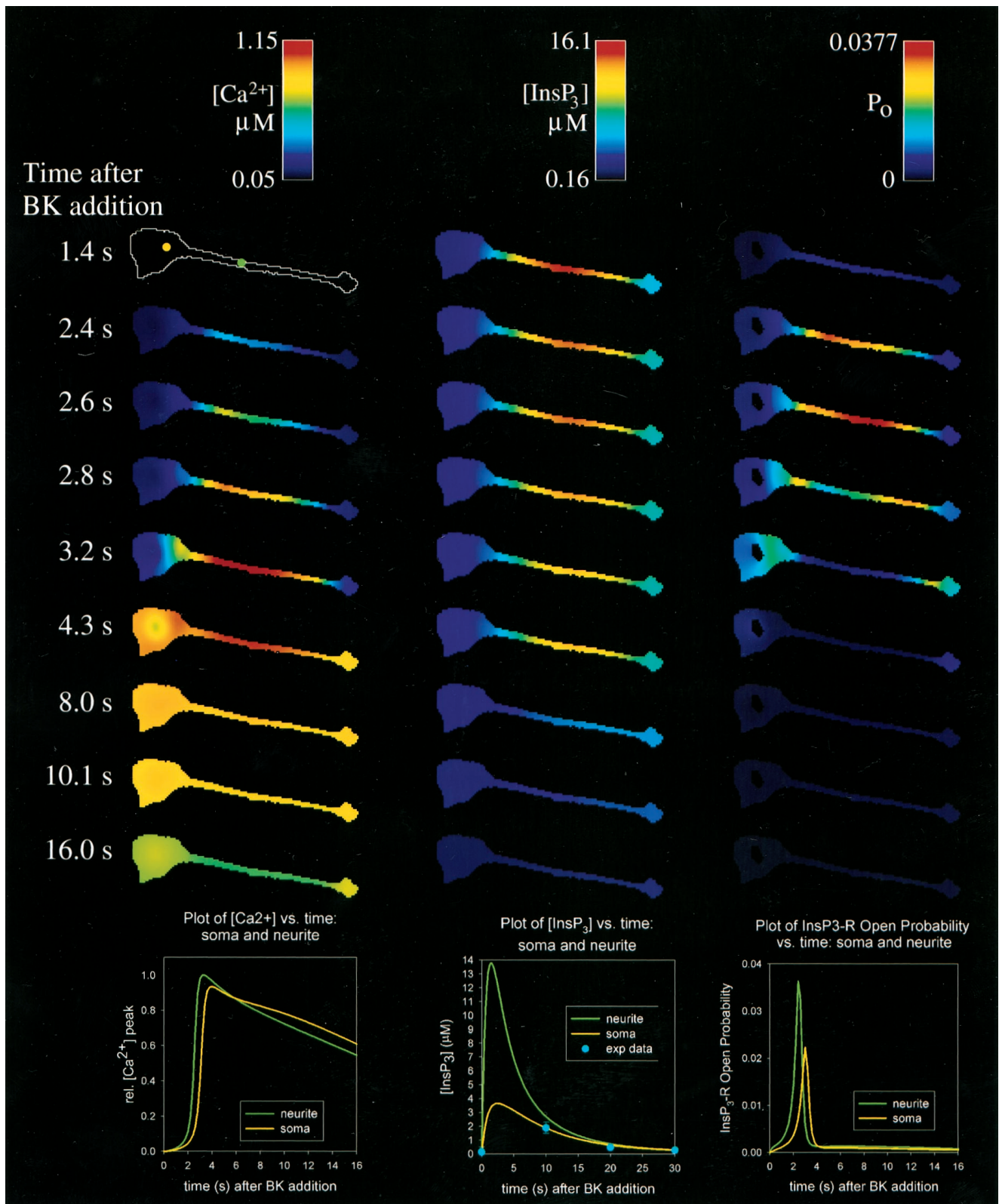| Region	Mean ER Distribution	ER SE	ER SD	Mean BKR Distribution	BKR SE	BKR SD
Outer soma	1.00	0.00	0.00	1.00	0.00	0.00
Inner soma	1.03	0.02	0.13	1.16	0.03	0.13
Proximal neurite	0.67	0.04	0.25	2.36	0.16	0.72
Mid neurite	0.60	0.04	0.24	2.45	0.22	0.97
Distal neurite	0.58	0.04	0.23	1.79	0.18	0.81
Growth cone	0.53	0.04	0.23	0.95	0.09	0.38

FIGURE 4 Simulation of BK-induced calcium wave using parameters illustrated in Fig. 3 *b*. From left to right columns, pseudocolored images show simulation results for $[Ca^{2+}]_{cyt}$, $[InsP_3]_{cyt}$, and P_O (the probability of opening of the InsP$_3$-R). At the bottom of each column, values in the soma and neurite (indicated by the *yellow* and *green dots* in the 1.4 s $[Ca^{2+}]_{cyt}$ image) are plotted against time. For the $[InsP_3]_{cyt}$ versus time plot, experimentally determined data (*filled cyan circles*) are superimposed onto the simulation data.

to achieve a near-perfect match. These "best fit" results can be seen in the first column of Fig. 5 *a*. The initiation point of the calcium wave and the $[Ca^{2+}]_{cyt}$ versus time plots for points in the soma and neurite in this simulation are virtually perfect matches to the experiment.

Using simulations to make experimentally testable predictions

A true test of the usefulness of a model is if it makes experimentally testable predictions. If the prediction proves to be incorrect, a reevaluation of the model would be required. If the predictions are consistent with experiment, the model acquires additional credibility and may be sufficient to describe the physiology.

To examine the role of calcium buffering, simulation results are shown (Fig. 5 *a*) for a BK-induced calcium wave in a cell with an additional calcium buffer, 100 μM CG-1 conjugated to a 10-kD dextran. The diffusion coefficient for this molecule is taken as 18.4 μm^2 s^{-1} and the K_D is 260 nM. In the second column of Fig. 5 *a*, the simulated calcium wave with additional CG can be compared to the best fit simulation in the first column. Now the peak $[Ca^{2+}]$ occurs much later ($\sim$12 s) and the amplitude is lower (0.68 vs. 1.16
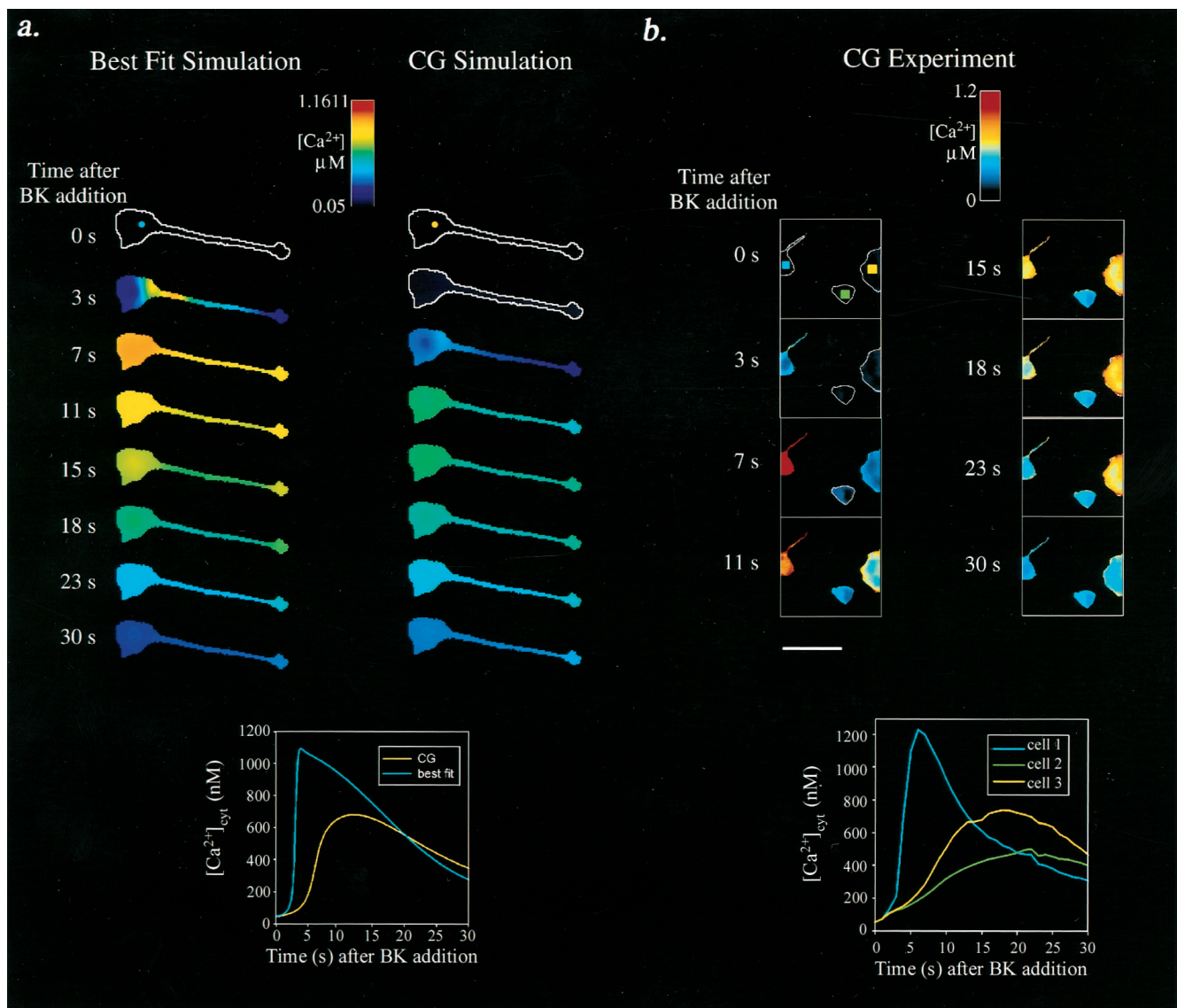

FIGURE 5 (*a*) Best-fit calcium simulation results for the cell shown in Fig. 1 (first column) and best fit simulation with 100 μM additional CG-10 kD dextran (second column). $[Ca^{2+}]_{cyt}$ versus time is plotted below for points in the soma (*cyan* and *yellow circles* in the 0 s images). (*b*) Experimental results of a BK-induced calcium wave for three cells: cells 2 and 3 have been microinjected with 100 μM CG-10 kD dextran. Cells were loaded with fura-2/AM; 340/380-nm ratio pairs were collected every second, and converted to $[Ca^{2+}]$. $[Ca^{2+}]_{cyt}$ versus time is plotted below for regions of interest in the somas (*cyan, green,* and *yellow rectangles* in the 0 s images). Scale bar = 100 μm.

μM) than the "best fit" simulation. An experimental example testing this prediction is shown in Fig. 5 *b*. All cells on this coverslip have been preloaded with fura-2/AM, but only cells 2 and 3 (highlighted by the *green* and *yellow squares* in the 0 s image) additionally contain $\sim$100 μM of microinjected CG-1. In this field of view, cell 1 (*cyan square*) acts as a control for the calcium response without added buffer. Cell 1 shows a calcium response typical for N1E-115 Nb cells, and is highly consistent with the cell shown in Fig. 1. By contrast, cells 2 and 3 are much slower to reach peak $[Ca^{2+}]$ ($>$15 s) and have significantly lower $[Ca^{2+}]$ amplitudes (700 and 500 nM vs. 1200 nM), consistent with the predictions in Fig. 5 *a*. Similar experiments were performed with 13 cells of varying CG-1 concentrations; in every case, the $[Ca^{2+}]$ response was significantly dampened when compared to control cells.

To examine the consequences of uniform InsP$_3$ production throughout the cytosolic volume, we simulated an InsP$_3$ uncaging experiment (Fig. 6 *a*). Key features of the predicted calcium response were a very brief latency ($<$2 s), calcium increase throughout the entire cell rather than a wave, and a lower $[Ca^{2+}]$ amplitude in the neurite compared to the soma. This results from the uneven distribution of ER (calcium stores) (see below for a "thought experiment" in which the ER is set to a uniform distribution throughout the cell). Fig. 6 *b* shows an experiment where $[Ca^{2+}]_{cyt}$ is imaged while 3 μM InsP$_3$ is uncaged uniformly throughout the cell, resulting in a simultaneous and uniform increase in InsP$_3$ throughout the cell volume. The calcium increase had a short latency, with no wave formation, and a significantly higher $[Ca^{2+}]$ in the soma than in the neurite. This result was repeatable in several experiments; on average, the peak $[Ca^{2+}]$ in the neurite was only 47 $\pm$ 5% of the soma (mean $\pm$ SE; n = 16 cells). These results contrast with the BK-induced calcium wave, where the peak $[Ca^{2+}]_{cyt}$ is approximately equal in the soma and neurite. One can reason that for a BK-induced calcium wave to have equal $[Ca^{2+}]_{cyt}$ amplitudes in the soma and neurite, the $[InsP_3]_{cyt}$ in the neurite must be higher than that of the soma.

Using simulations for questions not experimentally testable

Having demonstrated that the model can be used to make experimentally testable predictions, we now turn to thought experiments that can provide additional insights into the factors controlling the salient features of the BK-induced $[Ca^{2+}]_{cyt}$ response. Fig. 7 summarizes simulations used to observe calcium dynamics under conditions that would be difficult or impossible to establish experimentally. Column 1 of the figure contains the calcium dynamics for the best fit model for comparison to the other conditions represented in the other columns. The relative importance of BKR and ER distributions for determining the initiation point of the calcium wave can be explored by simulations in which the

distribution of these elements is made uniform. In column 2, BKR distribution is made uniform, while all other parameters remain unchanged from the best fit model. The amplitude of peak $[Ca^{2+}]$ is slightly lower (0.96 vs. 1.16 μM) and the latency is slightly longer. Overall, the calcium wave is qualitatively very similar to the best fit. ER distribution is made uniform in column 3, and while the peak $[Ca^{2+}]$ is still close to the best fit, there are notable differences. The calcium wave doesn't fully propagate into the soma, with $[Ca^{2+}]$ in the soma being only half that of the neurite. Also, the calcium wave initiates in the thinnest region of the cell rather than the neurite proximal to the soma. From these simulations and the results of InsP$_3$ uncaging in Fig. 6 we can conclude that the initiation point of the calcium wave is determined by the cell's morphology (i.e., an interplay of the regional differences in surface-to-volume ratio and intracellular distribution of the ER calcium stores). The uneven distribution of BKR established in Fig. 3 *b* appears to have a minor influence on calcium wave dynamics, serving primarily to focus the initiation point.

Modeling allows us to assess the perturbing effect of the calcium indicator (in this case, fura-2) on the calcium wave. Column 4 of Fig. 7 shows that in the absence of the indicator, maximal $[Ca^{2+}]_{cyt}$ is higher (2.08 vs. 1.16 μM) and wave initiation and propagation are more rapid (latency $\sim$0.5 s). It should be emphasized that the best fit model includes a fura-2 concentration of 75 μM that is experimentally determined from a series of measurements on individual cells (Fink et al., 1998). This concentration was the minimum required to achieve a practical signal-to-noise level in our calcium dynamics experiments. That fura-2 should perturb the calcium dynamics is not surprising because of its significant buffering capacity at the concentrations used for imaging experiments. However, the dramatic extent of this perturbation on both the amplitude and the time course of the $[Ca^{2+}]_{cyt}$ demonstrated by this simulation is generally not fully appreciated.

Diffusion of InsP$_3$ from the inner surface of the plasma membrane to its receptor on the ER membrane is clearly a critical prerequisite for the release of calcium. The diffusion of calcium may also be a crucial element in the propagation of many calcium waves because of the operation of calcium-dependent feedback mechanisms. Indeed, such feedback steps are included in the kinetic scheme for the InsP$_3$R (De Young and Keizer, 1992; Li and Rinzel, 1994) used in our model. Modeling allows us to test for the importance of calcium diffusion in controlling calcium wave propagation in the N1E-115 Nb cells by simply setting the calcium diffusion coefficient to 0 (Fig. 7, column 5). This simulation also includes removal of fura-2 because, as a mobile buffer, it can very effectively act to spread calcium throughout the cell. Remarkably, the calcium wave appears relatively unchanged from the simulation with just fura-2 absent (column 4). This argues that calcium diffusion has little influence on propagation of the calcium wave in N1E-115 Nb
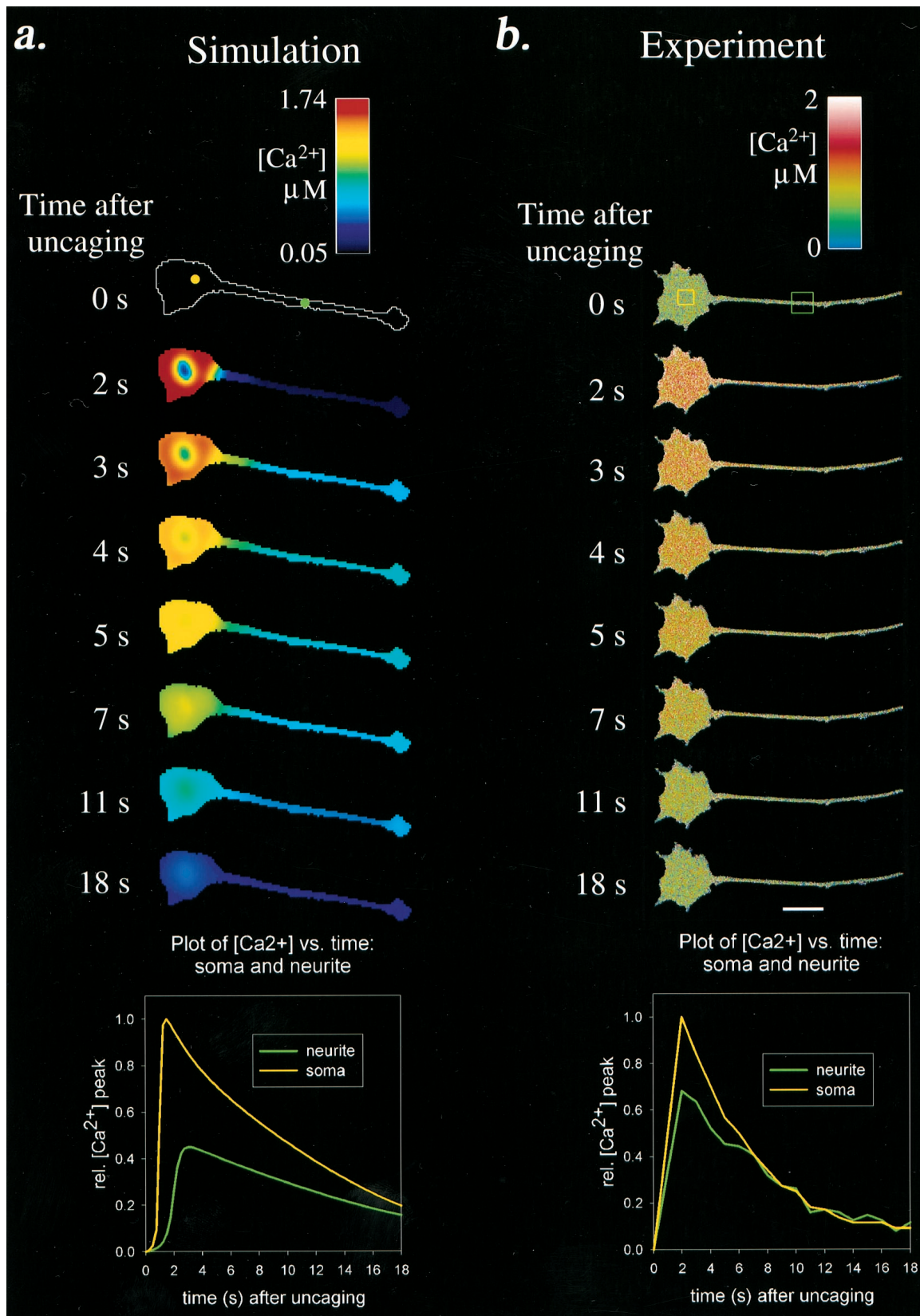
FIGURE 6 Simulation (*a*) and experimental (*b*) results for global uncaging of 3 μM InsP$_3$. Cells were microinjected with CG-1 (10 kD dextran) and NPE-InsP$_3$, and CG-1 fluorescence was measured on the confocal microscope. Uncaging was accomplished by rapid scanning with 364-nm laser light. $[Ca^{2+}]_{cyt}$ versus time is plotted below for regions of interest in the soma (*yellow*) and neurite (*green*). Scale bar = 25 μm.
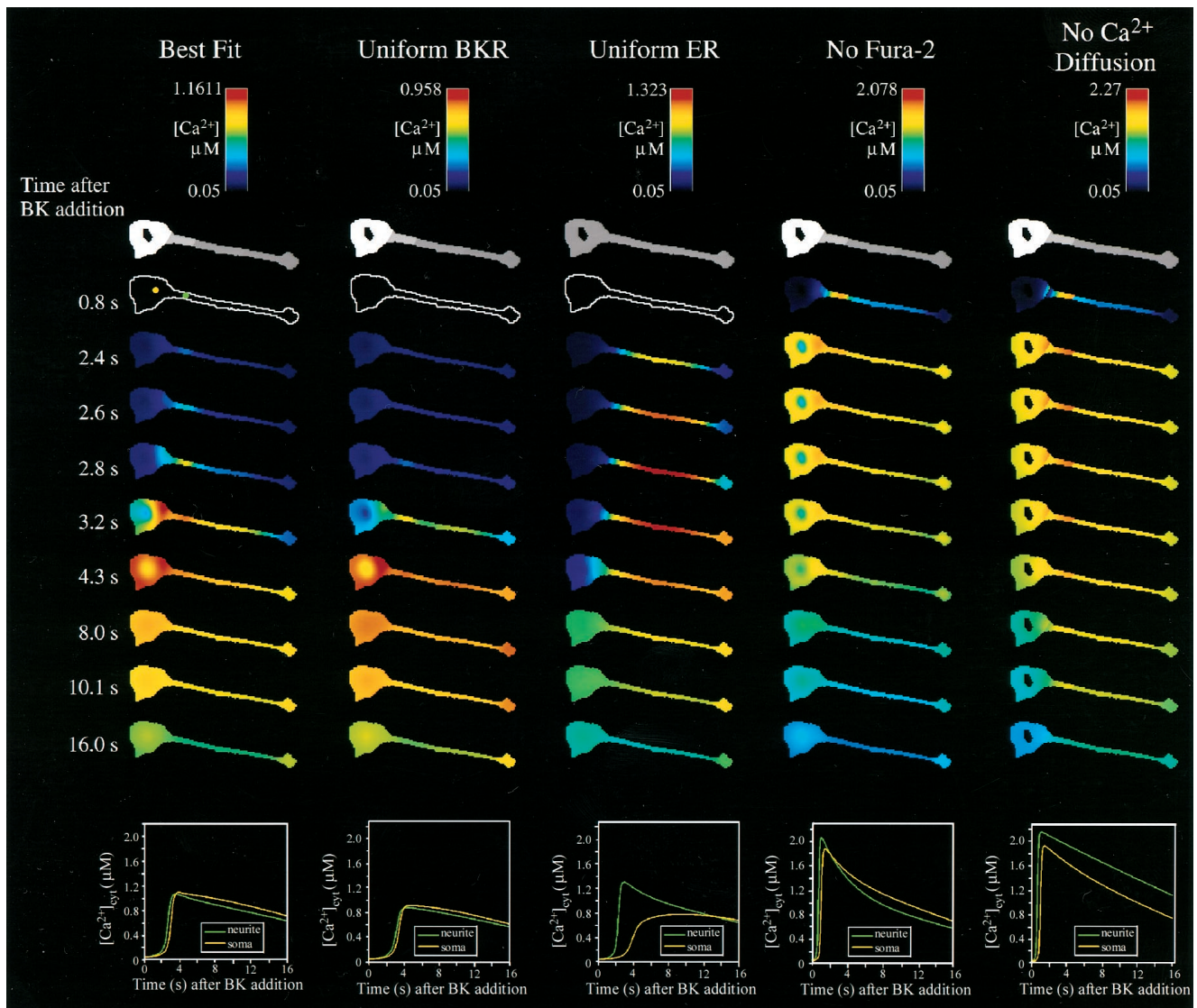
FIGURE 7   Simulation results for $[Ca^{2+}]_{cyt}$ following stimulation by external application of 500 nM BK. Simulations were run for the best-fit parameters (to match experimental results from Fig. 1), and four variations of this simulation (with all other features being identical): uniform BKR distribution across the plasma membrane, uniform ER (and InsP$_3$-R/SERCA2) distribution throughout the cytosol, absence of calcium indicator (fura-2), and no calcium diffusion (which entails the absence of calcium indicator along with setting the diffusion coefficient of calcium to zero). $[Ca^{2+}]$ has been pseudocolor-scaled with each column so that the maximum value is red. The first row shows the ER distribution that pertains to each column (compare with Fig. 3 *b*). Below each column are plots of $[Ca^{2+}]_{cyt}$ versus time for a point in the soma or neurite (indicated by the *yellow* or *green dots* on the 0.8 s image of the first column).

cells. Instead, we hypothesize the spatial pattern of InsP$_3$ generation and diffusion dictates the observed pattern of calcium release throughout the cell.

Experiments and simulations with alternate geometries

Finally, we performed simulations of the calcium wave in two Nb cells with very different geometries from the cell in Fig. 1. The latter has a generic neuronal morphology, with soma, a single neurite, and growth cone. Other than geometry (including changes in surface-to-volume corrections for

the 2D simulation), these simulations use exactly the same parameters as in previous simulations. If our modeling of calcium dynamics in N1E-115 Nbs is valid, then simulations of cells with alternate geometries should still be similar to experiments. The effects of cellular morphology on calcium waves are illustrated in Fig. 8. For a bipolar Nb, the simulation is an excellent match to the experiment (Fig. 8 *a*). For this simulation, a symmetrical model of the "average" distribution shown in Fig. 2 *b* was used: both neurites contain ER and BKR distributions equivalent to those shown for the single neurite in Fig. 2 *b*, while the center of the soma is assigned a relative density of unity.
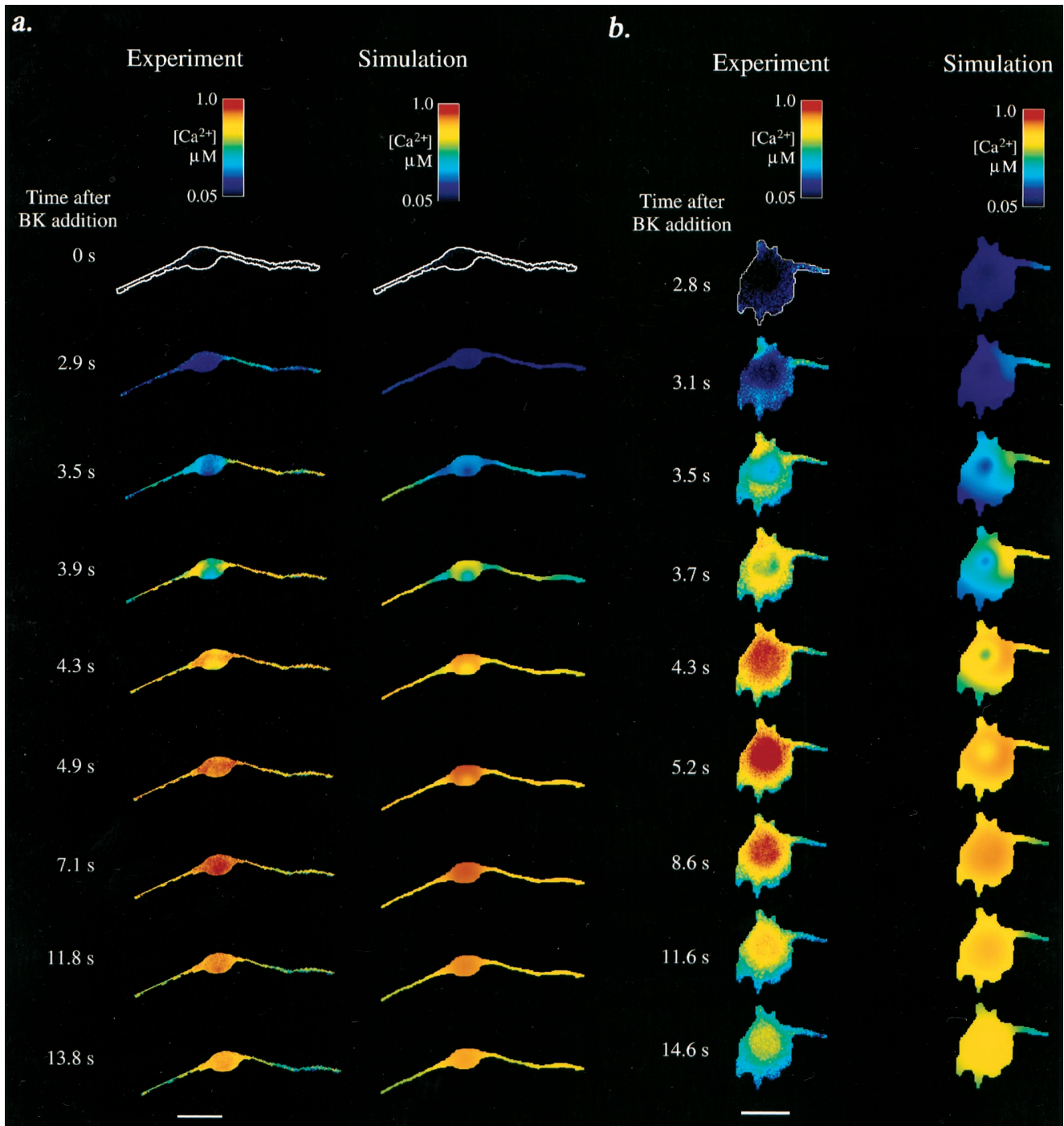
FIGURE 8   Experimental and simulated BK-induced calcium release in N1E-115 Nb cells of differing morphology. Cells were loaded with fura-2 and imaged as in Fig. 1. (*a*) Intracellular distributions were modeled as in Fig. 2 *b*, but with two neurites instead of one. (*b*) BKR and ER were modeled as having uniform distributions throughout the cell except for the small fingerlike nascent neurite, which was assigned lower ER densities consistent with Fig. 2 *b*. Scale bars = (*a*) 50 μM and (*b*) 20 μM.

An aster-shaped Nb cell is modeled in Fig. 8 *b*. To model this geometry, the BKR distribution was made uniform and the ER density in the periphery was set to 60% of a central circle. Of course, the nuclear region is kept void of ER. The fit of simulation to experiment for this cell is not perfect, but

the general behavior of calcium dynamics following BK stimulation is qualitatively similar. Initiation of the calcium wave occurs at ~3 s after BK stimulation. The point of calcium wave initiation is in a thin neurite-like protrusion on the right hemisphere of the cell, and the calcium wave

proceeds to spread radially inward. The major deviations from experiment seen in the simulation are a lower $[Ca^{2+}]_{cyt}$ in the soma and a slower rate of recovery to basal $[Ca^{2+}]_{cyt}$. Low $[Ca^{2+}]_{cyt}$ in the soma most likely results from nucleus having more relative volume in two dimensions than it would in three. The slow $[Ca^{2+}]_{cyt}$ recovery rate could be attributable to a number of modeling parameters that are altered slightly in cells of this geometry. Presumably, a perfect fit could also be obtained for these simulations, by modifying selected parameters to reflect population variances.

DISCUSSION

In N1E-115 Nb cells, saturating levels of BK are seen to stimulate robust and reproducible calcium waves that always follow the geometric pattern of initiating in the neurite and propagating to the growth cone and soma, with recovery also following the same sequence. Calcium waves are a common cellular mechanism for transducing signals from external stimuli, and different types of calcium waves are produced to elicit different downstream responses (Jaffe, 1993; Li et al., 1998). Within a single cell, different agonists can activate the same second messenger cascade while eliciting different calcium responses (Xu et al., 1996). How does a particular agonist trigger a specific cellular calcium response? Possibilities include differential location of plasma membrane receptors, InsP$_3$ receptors, and calcium stores. For BK-induced calcium waves in N1E-115 Nbs, we addressed this question by performing a series of calcium imaging experiments along with modeling within the VC computational environment. Experiments were compared with their simulation counterparts to validate our model and explore whether results from simulations can be used to achieve an understanding of the cellular physiology that couldn't be attained from experiment alone.

To construct a model capable of accurate reproduction of BK-induced calcium dynamics in N1E-115 Nbs, results from our experimental measurements and the existing literature were used. Cell geometry is taken from real images. Intracellular distributions for BKR, SERCA2, InsP$_3$-R, and ER calcium stores were determined by analysis of immunofluorescence. An average distribution profile for each of these was determined by analysis of 3D images of N1E-115 Nbs. Relative fluorescence intensity was corrected accounting for contributions from out-of-focus light. The amount of correction required for a given geometry was determined by analysis of primitive volumetric geometries that approximated the cellular geometry. These primitive volumetric geometries were convoluted according to a point spread function collected under experimental conditions. In previous work we demonstrated this procedure in detail (Fink et al., 1998). Concentrations of exogenous calcium buffers (fura-2 and CG-1) were determined in a similar manner. The time course of $[InsP_3]_{cyt}$ was determined biochemically

from entire populations of cells, and therefore provide no spatial resolution and poor temporal detail (10-s intervals). The levels of InsP$_3$ were consistent with those derived from quantitative release of caged InsP$_3$ (Fink et al., 1999b). $[Ca^{2+}]_{cyt}$ dynamics were measured with high spatial and temporal resolution, and were the major criteria for judging the quality of fit of the simulation. A number of parameters were taken from the literature, such as diffusion coefficients, channel and pump kinetics, and endogenous buffers. Because these values were sometimes derived from experiments with different cell lines and experimental conditions, these parameters were constrained to within a range consistent with our own system. Indeed, although we attempt to construct the model with parameter values derived from our own experiments or the related literature, the complexity of the system necessarily left us with some flexibility in assigning values to some of the parameters. However, the ability of the model to predict the results of experiments gives us confidence in the overall usefulness of the model. In particular, the model is able to predict

- The influence of added mobile buffer on the amplitude and dynamics of the calcium wave (Fig. 5);
- The altered spatial pattern of the calcium signal for InsP$_3$ uncaging (Fig. 6);
- The spatiotemporal pattern of calcium dynamics for cell morphologies very different from those of the unipolar cells used to develop the model (Fig. 8);
- The calcium response to focal applications of bradykinin to the soma, neurite, or growth cone (Fig. 4 of Fink et al., 1999b).

Why does the calcium wave always initiate in the neurite proximal to the soma? An initial hypothesis when confronted with such results would probably be to predict an uneven receptor distribution. Although the BKR distribution initially seemed strikingly correlated with the initiation point of the calcium wave, the simulations indicate that it serves primarily to help focus the initiation site (compare columns 1 and 2 in Fig. 7). The ER distribution was demonstrated to bias the initiation point toward the soma, where ER is most dense. The other primary factor is the high surface-to-volume ratio in the thinnest part of the cell, where the highest amplitude and most rapid InsP$_3$ accumulation are predicted by the simulations. The interplay of these two factors causes the $[Ca^{2+}]_{cyt}$ initiation point to be in the neurite proximal to the soma. The hypothesis that $[InsP_3]_{cyt}$ amplitude is biased toward the neurite is supported by the uncaging experiments. When uniform $[InsP_3]_{cyt}$ is produced throughout the cell by global uncaging, $[Ca^{2+}]_{cyt}$ is significantly higher in the soma than in the neurite. Because the peak amplitude of $[Ca^{2+}]_{cyt}$ is uniform throughout the cell during a calcium wave, this suggests that $[InsP_3]_{cyt}$ in the neurite must be higher than in the soma. Therefore, the initiation point of the calcium wave is determined by an interplay of ER distribution and cellular mor-

phology. Furthermore, we have shown in a previous report (Fink et al., 1999b) that this initiation zone in the proximal segment of the neurite can be focally stimulated to generate a calcium response throughout the cell. Thus this region of the cell, analogous to the axon hillock in a neuron, is both necessary and sufficient for the propagation of $[Ca^{2+}]_{cyt}$ signals. Such morphological control of signaling (Fink et al., 1999b) may be a general phenomenon that could pertain to many spatially localized cellular events.

It is important to emphasize that the model presented here was developed as a result of several iterations that involved refinements through new experiments. An example related to the spatial components of the system nicely illustrates this interplay. After initially studying the experimental calcium wave and gathering data on the underlying biochemical and electrophysiological mechanisms, we built a model with the simplest possible set of assumptions, viz., that BKR was evenly distributed along the plasma membrane, the ER was uniformly distributed within the cytosol, and the SERCA and InsP$_3$R were both evenly distributed within the ER membrane. When the simulations resulting from this initial model failed to produce a pattern of $[Ca^{2+}]_{cyt}$ dynamics consistent with experiment, we were prompted to thoroughly examine the relevant distributions by quantitative microscope imaging, culminating in the geometric model illustrated in Fig. 3 *b*. This model produced a simulation with a good match to experiment, and underlined how the uneven ER distribution was critical to understanding the spatiotemporal pattern of the calcium signal. Thus, the initial failure of a model prompted new experiments that ultimately resulted in a more accurate representation of the system and a more satisfactory model.

Another example of how the modeling process prompted us to perform new experiments concerns the basal and stimulated InsP$_3$ levels in these cells. We initially based our model on estimates from the literature for the BK-induced InsP$_3$ signal (Wang et al., 1995), but these levels were too low to evoke calcium release in our simulations, given the measured buffer levels and other constraints in our model. We therefore carried out our own measurements using standard radioligand binding assays on a cell population. The basal InsP$_3$ concentration was measured to be ~15-fold higher than the previous estimate, and the maximum stimulated level was almost two orders of magnitude higher. These levels provided a sufficient stimulus for calcium release in the model and were later confirmed via quantitative InsP$_3$ uncaging experiments (Fink et al., 1999b). Indeed, it is noteworthy that an interesting pattern of diversity is emerging in the sensitivity of calcium release to $[InsP_3]_{cyt}$ in different cell types. In many peripheral cells InsP$_3$ increases in the range of a few hundred nanomolar are sufficient to release calcium (e.g., Luzzi et al., 1998; Fink et al., 1999a), but in neuronal cells there is accumulating evidence that tens of micromolar are required (Khodakah and Og-

den, 1993). Our neuroblastoma cells appear to be intermediate between these extremes.

An interesting finding (Fig. 7) is that the calcium indicator (in this case, fura-2) has a major influence on the observed $[Ca^{2+}]_{cyt}$; 75 μM fura-2 reduces the measured $[Ca^{2+}]_{cyt}$ by ~50% and significantly slows the onset and propagation of the calcium wave. Fura-2 is a calcium buffer with a K_D in the range experienced by the cell during the calcium wave (224 nM). That a high concentration of fura-2 would alter calcium dynamics is not surprising, but the amount of indicator used in our study is typical and the magnitude of the effect is significant. The buffering effect could alter the calcium dynamics in more serious ways, such as abolishing calcium oscillations or repetitive waves. As demonstrated here, the VC provides a tool to account for the buffering effects of indicators, and estimate physiologically relevant concentrations.

The InsP$_3$ and calcium-dependence of the calcium dynamics were also examined. The model of the InsP$_3$ receptor used in simulations requires cooperative binding of InsP$_3$ and calcium for channel opening, with additional calcium binding inactivating the channel (Li and Rinzel, 1994). Therefore, both InsP$_3$ and calcium are potentially important in mediating calcium wave dynamics. Simulations showed that calcium diffusion was not required for propagation of the calcium wave. Although this initially seems illogical, further analysis revealed that the appearance of a calcium wave was generated by the [InsP$_3$] gradient throughout the cell. Though calcium is still required for opening of the InsP$_3$-R, basal $[Ca^{2+}]$ was sufficient to support the calcium wave front. This is contrary to reports in other cell types, where calcium diffusion is hypothesized to mediate calcium wave propagation (Jaffe, 1993). However, recent experimental evidence in MDCK cells shows that an InsP$_3$ wave precedes the calcium wave (Hirose et al., 1999), consistent with our results. Because N1E-115 Nbs do not contain ryanodine receptor, calcium-induced calcium release (CICR) is not thought to play a role in calcium wave propagation. Instead, we hypothesize that the spatial and temporal pattern of $[InsP_3]_{cyt}$ dictates calcium dynamics. This is similar to the phase waves described by Sneyd, Keizer, and colleagues (Jafri and Keizer, 1995; Sneyd et al., 1995).

Some approximations were made to limit the size and spatial complexity of the model to improve computational efficiency. ER was modeled as a continuous network of varying density throughout the cytosol. This was necessary because modeling the fine structure of the reticular membrane would require much longer computational times (i.e., smaller mesh size). We have chosen to use a 2D geometry, albeit with plasma membrane surface-to-volume values corrected for three dimensions. This allowed for full simulations (16 s simulated time) to be completed in <15 min. Although calcium wave simulations in three dimensions are possible, the necessity for this does not justify the greatly increased computational time. One consequence of this compromise is that the nucleus, void of calcium stores, has

an effectively exaggerated size with respect to the rest of the soma because the ER that surrounds it dorsally and ventrally is missing. This has the effect of making simulated $[Ca^{2+}]$ in the soma somewhat lower than experimentally observed values (particularly noticeable in Fig. 8 b). These simplifications are not so severe, however, to affect the value of the model for helping us understand the calcium dynamics in Nb cells.

Simplifications were made to minimize the number of interacting molecular components within the model while maintaining the accuracy of the simulation. For example, membrane-localized signal transduction proteins that are known intermediates in InsP3 generation, such as G-proteins and phospholipase C (PLC), were not directly included. Instead, InsP3 production and degradation were modeled phenomenologically, at a rate consistent with our direct experimental measurements. Even though we did not determine intracellular distributions for components not modeled, local application of BK to various regions of the cell shows that a calcium increase can be stimulated anywhere (Fink et al., 1999b). Therefore, it is possible to initiate calcium release in all regions of the cell, suggesting that the required physiological machinery is available along the entire cell surface. Another simplification was calcium buffering within the ER. We used a value of 400 μM for $[Ca^{2+}]_{ER}$, consistent with measurements obtained from other cell types (Miyawaki et al., 1997; Meldolesi and Pozzan, 1998). However, bound and free $[Ca^{2+}]_{ER}$ have not been determined in these cells. For the purposes of the simulation we wanted a calcium source large enough to account for the observed calcium increase in the cytosol. As modeled here, the ER stores are not depleted during the calcium wave. However, this is not necessarily correct, and more detailed modeling can shed light on the consequences of this assumption. It would also be ideal to obtain intracellular distributions from the same cells for which $[Ca^{2+}]_{cyt}$ has been imaged. For this, green fluorescent protein (GFP) constructs to label receptors and organelles would be ideal. Another intriguing possibility is to implement different models of the InsP3 receptor (e.g., Mak et al., 1998). Because of its modular structure that separates the mathematics from the physiology and geometry (Schaff et al., 1999), the VC environment facilitates the editing of existing models to incorporate new features or modified hypotheses. Simulation results could suggest experiments that would discriminate between these different models.

Thus, it is important to emphasize that a model such as the one developed here is nothing more than a collection of hypotheses. As such, it is impossible to "prove" the accuracy or veracity of a model. Indeed, a model is most useful when its predictions fail to match experiment, as this can provide a clear guide to which hypotheses within the model require revision or augmentation. As noted above, this investigation of BK-induced calcium dynamics in the differentiated N1E-115 Nb cells offers several examples of such an interplay between modeling and experiment. Although

the components of this model can prove to be useful starting points for the construction of models of calcium dynamics in other cell types, the diversity of the molecules involved in signaling pathways requires that a similar process of give and take between modeling and experiment will be necessary.

In summary, BK-induced calcium waves in N1E-115 Nb cells have been characterized for their initiation site, velocity, propagation pattern, and recovery. Of particular interest is the fact that the initiation site was always in the neurite, subsequently propagating to the soma and distal neurite/growth cone. Simulations were performed using VC, an image-based modeling system, based on the known and estimated concentrations and kinetics of factors thought to play a role in mediating the calcium wave phenomena. Results from the simulations support the hypothesis that an interplay of cell shape (surface-to-volume ratio of neurite versus soma) and intracellular distribution of ER is sufficient to explain the pattern of calcium release. There is high fidelity between the simulation and the experimental calcium waves. The model is further validated by using the simulations to make experimentally testable predictions, and by examining cells with varying morphologies. The ability to experimentally estimate inaccessible components (such as $[InsP_3]_{cyt}$ and open probability of the InsP3-gated channel) is a power of the simulations. Also, questions that are impossible or highly difficult to answer with experiment can be approached with models. The close interdependence of experiment and model development is a key strength of the image-based spatial modeling that is demonstrated in this work.

APPENDIX

InsP3 dynamics

InsP3 dynamics accounts for its production at the plasma membrane, diffusion into the cytosol, and gradual degradation (Allbritton et al., 1992). InsP3 production is modeled by imposing an appropriate boundary condition at the plasma membrane for the flux density:

$$j_{IP_3} = J_{IP_3} \exp(-k_0 t). \qquad (1)$$

Equation 1 corresponds to a very rapid (practically instantaneous on the time scale of interest) increase in InsP3 production immediately after the BK application and the following exponential decay with the time constant k_0. The flux density amplitude J_{IP_3} is generally a function of spatial variables because of a nonuniform distribution of BK receptors. Because this is a 2D simulation, this value was also corrected for the difference of surface-to-volume ratios between the soma and neurite regions in the actual 3D cell geometry. See Reduction of the Model to Two Dimensions (below) and Fig. 3 for information on the spatial distribution of the flux density amplitude that was actually used in the simulations. The average value of J_{IP_3} and the time constant k_0 value (see Table 2) were picked to correctly reproduce the experimentally observed time course of the average InsP3 concentration.

Diffusion and degradation of InsP3 are described by the equation

$$\frac{\partial [IP_3]}{\partial t} = D_{IP_3} \nabla^2 [IP_3] - k_{degr}([IP_3] - [IP_3]_0), \qquad (2)$$

which, together with the flux jump condition (Eq. 1), provides the full description of the InsP$_3$ dynamics in our model. The values of the diffusion constant D_{IP_3}, the degradation rate k_{degr}, and the basal InsP$_3$ level at $t = 0$, $[IP_3]_0$, are also given in Table 2.

Note that different membrane conditions and initial conditions are used to model the InsP$_3$ uncaging experiments. In this case, $j_{IP_3} = 0$ and the InsP$_3$ concentration at time $t = 0$ (immediately after UV flash) is assumed to be $[IP_3]_0 + [IP_3]_{max}$, where $[IP_3]_{max}$ is the uncaged amount of InsP$_3$.

ER

We use a continuous approximation in our modeling of ER. This assumption should provide an accurate description within the resolution limits of the light microscope used to record Ca^{2+} dynamics. As an internal calcium store, ER is considered to have an infinite capacity and, therefore, is characterized by a constant free calcium concentration $[Ca]_{ER}$.

The ER distribution in a cell is not uniform. The experimental data indicate that the InsP$_3$ receptor density and the pump density are considerably higher in the soma and experience a sharp decrease at the junction with the neurite (see Fig. 3 b). We use these experimental data to modulate the average rate of change of calcium concentration due to fluxes through the calcium channels and pumps. The actual function of spatial variables shown in Fig. 3 b was used in the simulations as described below in Reduction of the Model to Two Dimensions.

Calcium dynamics

The calcium dynamics is governed by the partial differential equation (Sneyd et al., 1995),

$$\frac{\partial [Ca]}{\partial t} = D_{Ca} \nabla^2 [Ca] + \alpha(J_{channel} - J_{pump} + J_{leak}) + R_{buffering},$$

(3)

that takes into account effects of calcium release from ER through the InsP$_3$-sensitive channels, leak, and uptake by the SERCA pumps combined with calcium diffusion and buffering. $J_{channel}$, J_{pump}, and J_{leak} are the rates of change of calcium concentration due to the channel release, pump uptake, and leak, respectively. The factor α is a function of spatial coordinates that modulates calcium fluxes due to the nonuniform ER distribution (see Reduction of the Model to Two Dimensions and Fig. 3). $R_{buffering}$ is the rate of change of calcium concentration due to buffering. Our treatment of calcium buffering is based on the rapid buffer approximation. (Wagner and Keizer, 1994) and is described below in Calcium Buffering.

Equation 3 is accompanied by a jump membrane condition (see Eq. 9 below) that accounts for the plasma membrane extrusion mechanisms. The initial calcium distribution is assumed uniform.

Channel kinetics

We use the simplified version (Li and Rinzel, 1994) of the model proposed by De Young and Keizer (1992) to describe the calcium release through an InsP$_3$-sensitive channel:

$$J_{channel} = J_{max} \left(\left(\frac{[IP_3]}{[IP_3] + K_{IP_3}} \right) \left(\frac{[Ca]}{[Ca] + K_{act}} \right) h \right)^3 \left(1 - \frac{[Ca]}{[Ca]_{ER}} \right),$$

(4)

where J_{max} is the maximal possible rate; K_{IP_3} is the dissociation constant for InsP$_3$ binding to a channel; K_{act} is the dissociation constant for calcium binding to an activation site; $[Ca]_{ER}$ is the calcium concentration in ER; h is the probability of the inhibition site being not occupied, and the gov-

erning equation for h is

$$\frac{\partial h}{\partial t} = k_{on}(K_{inh} - ([Ca] + K_{inh})h),$$

(5)

where k_{on} is the on-rate of calcium binding to the inhibition site and K_{inh} is the corresponding dissociation constant.

SERCA pump kinetics

The SERCA pump uptake is modeled as a pseudo-steady state process with respect to Ca^{2+} binding and described by a Hill-type equation (Gill and Chueh, 1985; Lytton et al., 1992),

$$J_{pump} = V_{max} \frac{[Ca]^2}{[Ca]^2 + K_p^2},$$

(6)

where V_{max} is the maximal rate and K_p is the corresponding dissociation constant. The constant values are given in Table 3.

Leak

The rate of change of the calcium concentration due to calcium leak from ER to the cytosol is modeled as

$$J_{leak} = L\left(1 - \frac{[Ca]}{[Ca]_{ER}}\right),$$

(7)

where the leak constant L is to be determined from the conditions of a flux balance at a steady state. The initial steady-state values of variables are

$$[Ca]_0 = 0.05 \ \mu M, \quad h_0 = \frac{K_{inh}}{[Ca]_0 + K_{inh}}.$$

Calcium buffering

Calcium buffering has a significant impact on the overall calcium dynamics. The endogenous buffers are usually assumed to be practically stationary with the binding ratio $B_s^{tot}/K_s \approx 40.0$ (B_s^{tot} is the total buffer concentration, and K_s is its dissociation constant) and the on-rate of the order of $5.0 \times 10^8 \ M^{-1}s^{-1}$ (Xu et al., 1997). Taking into account typical values of B_s^{tot}, we arrive at very short characteristic times of buffering. The presence of a small parameter makes it possible to apply the pseudo-steady approximation (Wagner and Keizer, 1994) when the bound buffer is considered to be in a rapid equilibrium with the local calcium. The fluorescent dyes used in the simulated experiments (fura-2 in BK experiments and Calcium Green in uncaging experiments), also act as rapid buffers, but are mobile in contrast with the endogenous buffers. Correspondingly, we introduced two types of buffers in our simulations: the stationary buffer B_1, representing endogenous buffers, and the mobile buffer B_2, modeling fluorescent indicators. The term $R_{buffering}$ from Eq. 3 then takes a form

$$R_{buffering} = R_1 + R_2$$

where

$$R_1 = -k_{1,on}[Ca][B_1] + k_{1,off}[CaB_1],$$

and

$$R_2 = -k_{2,on}[Ca][B_2] + k_{2,off}[CaB_2]$$

and the variables $[B_1]$, $[B_2]$, $[CaB_1]$, and $[CaB_2]$ are governed by the

equations

$$\frac{\partial[B_1]}{\partial t} = -\frac{\partial[CaB_1]}{\partial t} = R_1, \quad (8a)$$

$$\frac{\partial[B_2]}{\partial t} = D_{\text{buffer}}\nabla^2[B_2] + R_2, \quad (8b)$$

$$\frac{\partial[CaB_2]}{\partial t} = D_{\text{buffer}}\nabla^2[CaB_2] - R_2. \quad (8c)$$

Our numerical approach to fast buffering (and, generally, to any fast reactions in biochemical systems) is based on the combination of time-splitting and the pseudo-steady approximation applied to fast reactions (Slepchenko et al., 2000). Time-splitting allows us to separate slow and fast processes and use different methods for their treatment. No preliminary analytical manipulation is necessary. Because fast buffering is treated within a pseudo-steady approximation, the algorithm does not require information about the kinetic constants of fast buffering. All we need to describe fast reactions are equilibrium constants

$$K_1 = \frac{k_{1,\text{off}}}{k_{1,\text{on}}}, \quad K_2 = \frac{k_{2,\text{off}}}{k_{2,\text{on}}},$$

and total buffer concentrations $[B_1]_{\text{tot}}$, $[B_2]_{\text{tot}}$ (see Table 4).

Plasma membrane extrusion mechanisms

This type of calcium extrusion (through plasma membrane pumps and Na^+-Ca^{2+} exchangers) is important for the correct description of calcium distribution in a cell during the refractory phase of the calcium signal. According to the experimental data (Herrington et al., 1996), the corresponding flux, as a function of the cytosolic calcium, exhibits a threshold behavior. There is no flux below the critical concentration $[Ca]_c$, while above this concentration the flux grows linearly as a function of $[Ca]$. Thus, we introduce the following flux membrane condition for calcium:

$$j_{Ca} = \begin{cases} \gamma([Ca] - [Ca]_c), & \text{if} \quad [Ca] \geq [Ca]_c \\ 0, & \text{if} \quad [Ca] \leq [Ca]_c \end{cases} \quad (9)$$

where the rate of flux density γ is generally a function of spatial variables depending on the distributions of the plasma membrane pumps and exchangers. These distributions were assumed uniform in our simulations. Similar to the description of InsP$_3$ fluxes (see Reduction of the Model to Two Dimensions), the correction of γ was made due to the difference of actual 3D surface-to-volume ratios of the soma and the neurite.

Reduction of the model to two dimensions

The analysis of the cell geometry (Fig. 1) indicates that, though the average surface-to-volume ratio of the 2D model $\sigma = 0.263$ μm^{-1} is close to the actual 3D one, the corresponding values for the soma and the neurite are different. By taking the soma as a hemisphere and the neurite as a hemicylinder (accounting for the adhesive flattening of the cells on the coverslip), we were able to estimate appropriate adjustments for the two regions of the cell. Specifically, $(\sigma_n/\sigma_s)_{2D} = 3.63$, while $(\sigma_n/\sigma_s)_{3D} = 5.25$ (here and in the following the subscripts n and s denote values associated with the neurite and the soma, correspondingly). Because the surface-to-volume ratios are important for the overall dynamics, we need to make corresponding corrections of the membrane flux density distributions.

We first consider the InsP$_3$ flux density. Its amplitude J_{IP_3} in Eq. 1 can

be described as

$$J_{IP_3} = \beta \times \begin{cases} J_s, & \text{for the soma,} \\ J_n, & \text{for the neurite.} \end{cases} \quad (10)$$

The function β accounts for the experimentally determined nonuniform distribution of the BK receptors and is presented in the figure. To determine J_s and J_n in terms of the average flux density J_0, we note that

$$\delta = \frac{J_n}{J_s} = \left(\frac{\sigma_n}{\sigma_s}\right)_{3D} \bigg/ \left(\frac{\sigma_n}{\sigma_s}\right)_{2D} = 1.45 \quad (11a)$$

and

$$J_n(\sigma_n)_{2D}w_n + J_s(\sigma_s)_{2D}2_s = J_0\sigma, \quad (11b)$$

where w_n and w_s are the volume fractions of the neurite and soma in the 2D model, correspondingly. Solving Eqs. 11 simultaneously, we obtain

$$J_s = J_0\sigma(\delta(\sigma_n)_{2D}w_n + (\sigma_s)_{2D}w_s)^{-1}, \quad (12a)$$

$$J_n = J_0\sigma\delta(\delta(\sigma_n)_{2D}w_n + (\sigma_s)_{2D}w_s)^{-1}. \quad (12b)$$

Similar corrections should be made for the rate of calcium flux density γ in Eq. 9:

$$\gamma = \begin{cases} \gamma_s, & \text{for the soma,} \\ \gamma_n, & \text{for the neurite,} \end{cases} \quad (13)$$

where

$$\gamma_s = \gamma_0\sigma(\delta(\sigma_n)_{2D}w_n + (\sigma_s)_{2D}w_s)^{-1}, \quad (14a)$$

$$\gamma_n = \gamma_0\sigma\delta(\delta(\sigma_n)_{2D}w_n + (\sigma_s)_{2D}w_s)^{-1}. \quad (14b)$$

In Eqs. 12 and 14, $w_n = 0.377$, $w_s = 0.623$, $(\sigma_n)_{2D} = 0.479$ μm^{-1}, and $(\sigma_s)_{2D} = 0.132$ μm^{-1}. The average value of the rate γ_0 is given in Table 3. Finally, we define the function α of Eq. 3 as $\alpha = \alpha_0 f$, where $\alpha_0 = 1.41$, and the normalized ER density distribution f obtained in experiment (Fig. 3 b). The data for images corresponding to cells in Fig. 8, a and b are given in Table 5.

Numerical methods

The VC used the finite volume method (Patankar, 1980) for solving partial differential equations (PDEs), the forward Euler method for solving ordinary differential equations (ODEs), and the Newton method for solving the system of nonlinear equations for fast buffering (Press et al., 1992). The diffusion terms of PDEs are treated implicitly, while the reaction terms are treated explicitly. We solve the system of equations within the VC computational framework (Schaff et al., 1997). Based on an object-oriented approach, the framework provides convenient tools for creating all necessary compartments within an arbitrary geometry and all necessary variables within each compartment. It then builds up the discretized version of equations to be solved and uses PDE, ODE, or algebraic solvers where they are necessary. The solvers have been rigorously tested against exact solutions. The system of linear algebraic equations, obtained after the discretization of PDEs, is iteratively solved by the line-by-line method (Patankar, 1980) using six iterations for each dimension. We decomposed the 2D computational domain into 7.7×10^3 discrete volumes with 1.2 μm mesh size and ran simulations using a 0.01-s time step. The computations were performed on a variety of workstations; as an example, on a 500 Mhz Pentium III computer, the runtime was ~15 min per simulation. Comparing results obtained with various mesh sizes and time increments, we estimate that the computational error does not exceed 3%.

TABLE 2 InsP$_3$ dynamics

Parameter	Symbol	Value	Units	Reference
Average flux density amplitude	J_0	20.86	μM μm s^{-1}	Fit to experiment
Flux time constant	k_0	1.188	s^{-1}	Fit to experiment
Degradation rate	k_{degr}	0.14	s^{-1}	Wang et al., 1995, present work
Initial InsP$_3$ concentration	$[IP_3]_0$	0.16	μM	Experimentally determined
Uncaged amount of InsP$_3$	$[IP_3]_{max}$	3.0	μM	Experimentally determined
InsP$_3$ diffusion coefficient	D_{IP_3}	283	μm^2 s^{-1}	Allbritton et al., 1992

TABLE 3 ER and plasma membrane Ca^{2+} fluxes and diffusion

Parameter	Symbol	Value	Units	Reference
Average amplitude of channel release	J_{max}	3500	μM s^{-1}	Bezprozvanny et al., 1991; Kupferman et al., 1997; present work
Average amplitude of pump uptake	V_{max}	3.75	μM s^{-1}	Fit to experiment
Leak constant	L	0.1	μM s^{-1}	Determined by the steady-state balance
Dissociation constant for Ca^{2+} binding to an activation site	K_{act}	0.3	μM	Constrained by stability conditions
Dissociation constant for Ca^{2+} binding to an inhibition site	K_{inh}	0.2	μM	Constrained by stability conditions
On-rate for Ca^{2+} binding to an inhibition site	k_{on}	2.7	μM^{-1} s^{-1}	Fit to experiment
Dissociation constant for InsP$_3$ binding to a channel	K_{IP_3}	0.8	μM	Fit to experiment
Dissociation constant for Ca^{2+} binding to a pump	K_p	0.27	μM	Gill and Chueh, 1985; Lytton et al., 1992
Initial Ca^{2+} concentration	$[Ca]_0$	0.05	μM	From indicator fluorescence
Ca^{2+} concentration in ER	$[Ca]_{ER}$	400	μM	Miyawaki et al., 1997; Meldolesi and Pozzan, 1998
Average rate of Ca^{2+} flux density at the plasma membrane	γ_0	8.0	μm s^{-1}	Herrington et al., 1996, fit to experiment
Threshold concentration for calcium extrusion at the plasma membrane	$[Ca]_c$	0.2	μM	Herrington et al., 1996
Ca^{2+} diffusion coefficient	D_{Ca}	220	μm^2 s^{-1}	Klingauf and Neher, 1997

TABLE 4 Calcium buffering

Parameter	Symbol	Value	Units	Reference
Total concentration of stationary endogenous buffers (bound and unbound)	B_1	450	μM	Klingauf and Neher, 1997; Xu et al., 1997
Dissociation constant for Ca^{2+} binding to an endogenous buffer	K_1	10	μM	Klingauf and Neher, 1997
Total concentration of the exogenous buffer (BK experiments—Fura-2)	B_2	75.0	μM	Experimentally determined
Dissociation constant for Ca^{2+} binding to the exogenous buffer (Fura-2)	K_2	0.24	μM	Klingauf and Neher, 1997
Diffusion coefficient of the exogenous buffer (Fura-2)	D_{buffer}	50	μm^2 s^{-1}	Klingauf and Neher, 1997
Total concentration of the exogenous buffer (uncaging experiments—Calcium Green)	B_2	18.0	μM	Measured $[CG-1]_{cyt}$
Dissociation constant for Ca^{2+} binding to the exogenous buffer (Calcium Green)	K_2	0.26	μM	Eberhard and Erne, 1991
Diffusion coefficient of the exogenous buffer (Calcium Green)	D_{buffer}	18.4	μm^2 s^{-1}	Calculated based on diffusion of a sphere

TABLE 5 Reduction to 2D model

Parameters	Fig. 3 cell	Fig. 8a cell	Fig. 8b cell
Average surface-to-volume ratio σ_{2D} (μm^{-1})	0.263	0.473	0.126
Soma surface-to-volume ratio $(\sigma_s)_{2D}$ (μm^{-1})	0.132	0.171	—
Neurite surface-to-volume ratio $(\sigma_n)_{2D}$ (μm^{-1})	0.479	0.715	—
$\delta = ((\sigma_n/\sigma_s)_{3D})/((\sigma_n/\sigma_s)_{2D})$	1.45	1.172	—
Soma volume fraction w_s	0.623	0.444	1
Neurite volume fraction w_n	0.377	0.556	—
Soma flux correction factor J_s/J_0	0.768	1.023	—
Neurite flux correction factor J_n/J_0	1.106	0.873	—

REFERENCES

Allbritton, N. L., T. Meyer, and L. Stryer. 1992. Range of messenger action of calcium ion and inositol 1,4,5-trisphosphate. *Science.* 258: 1812–1815.

Atri, A., J. Amundson, D. Clapham, and J. Sneyd. 1993. A single-pool model for calcium oscillations and waves in the *Xenopus laevis* oocyte. *Biophys. J.* 65:1727–1739.

Benevolensky, D., I. Moraru, and J. Watras. 1994. Micromolar calcium reduces the affinity of the inositol 1,4,5-trisphosphate receptor in smooth muscle. *Biochem. J.* 299:631–636.

Bezprozvanny, I., J. Watras, and B. E. Ehrlich. 1991. Bell-shaped calcium-response curves of Ins(1,4,5)P$_3$- and calcium-gated channels from endoplasmic reticulum of cerebellum. *Nature.* 351:751–754.

Bray, D. 1997. Reductionism for biochemists: how to survive the protein jungle. *Trends Biochem. Sci.* 22:325–326.

Coggan, J. S., and S. H. Thompson. 1995. Intracellular calcium signals in response to bradykinin in individual neuroblastoma cells. *Am. J. Physiol. Cell Physiol.* 269:C841–C848.

Coggan, J. S., and S. H. Thompson. 1997. Cholinergic modulation of the Ca^{2+} response to bradykinin in neuroblastoma cells. *Am. J. Physiol. Cell Physiol.* 273:C612–C617.

De Young, G. W., and J. Keizer. 1992. A single-pool inositol 1,4,5-trisphosphate-receptor-based model for agonist-stimulated oscillations in Ca^{2+} concentration. *Proc. Natl. Acad. Sci. USA.* 89:9895–9899.

Eberhard, M., and P. Erne. 1991. Calcium binding to fluorescent calcium indicators: Calcium green, Calcium Orange, and Calcium Crimson. *Biochem. Biophys. Res. Commun.* 180:209–215.

Farooqui, A., D. Anderson, C. Flynn, and E. Bradel. 1990. Stimulation of mono- and diacylglycerol lipase activities by bradykinin in neural cultures. *Biochem. Biophys. Res. Commun.* 166:1001–1009.

Fink, C., F. Morgan, and L. M. Loew. 1998. Intracellular fluorescent probe concentrations by confocal microscopy. *Biophys. J.* 75:1648–1658.

Fink, C. C., B. Slepchenko, and L. M. Loew. 1999a. Determination of time-dependent inositol-1,4,5-trisphosphate concentrations during calcium release in a smooth muscle cell. *Biophys. J.* 77:617–628.

Fink, C. C., B. Slepchenko, I. I. Moraru, J. Schaff, J. Watras, and L. M. Loew. 1999b. Morphological control of inositol-1,4,5-trisphosphate-dependent signals. *J. Cell Biol.* 147:929–935.

Gill, D., and S.-H. Chueh. 1985. An intracellular (ATP + Mg^{2+})-dependent calcium pump within the N1E-115 neuronal cell line. *J. Biol. Chem.* 260:9289–9297.

Glanville, N., D. Byers, H. Cook, M. Spence, and F. Palmer. 1989. Differences in the metabolism of inositol and phosphoinositides by cultured cells of neuronal and glial origin. *Biochim. Biophys. Acta.* 1004:169–179.

Grynkiewicz, G., M. Poenie, and R. Y. Tsien. 1985. A new generation of Ca^{2+} indicators with greatly improved fluorescence properties. *J. Biol. Chem.* 260:3440–3450.

Herrington, J., Y. B. Park, D. F. Babcock, and B. Hille. 1996. Dominant role of mitochondria in clearance of large Ca^{2+} loads from rat adrenal chromaffin cells. *Neuron.* 16:219–228.

Higashida, H., and D. Brown. 1987. Bradykinin inhibits potassium (M) currents in N1E-115 neuroblastoma cells. *FEBS Lett.* 220:302–306.

Hirose, K., S. Kadowaki, M. Tanabe, H. Takeshima, and M. Iino. 1999. Spatiotemporal dynamics of inositol 1,4,5-trisphosphate that underlies complex Ca^{2+} mobilization patterns. *Science.* 284:1527–1530.

Iredale, P., K. Martin, S. Hill, and D. Kendall. 1992. Agonist-induced changes in [Ca^{2+}]$_i$ in N1E-115 cells: differential effects of bradykinin and carbachol. *Eur. J. Pharmacol.* 226:163–168.

Jaffe, L. 1993. Classes and mechanisms of calcium waves. *Cell Calcium.* 14:738–745.

Jafri, M. S. 1995. A theoretical study of cytosolic calcium waves in *Xenopus* oocytes. *J. Theor. Biol.* 172:209–216.

Jafri, M. S., and J. Keizer. 1995. On the roles of Ca^{2+} diffusion, Ca^{2+} buffers, and the endoplasmic reticulum in IP$_3$-induced Ca^{2+} waves. *Biophys. J.* 69:2139–2153.

Keizer, J., and G. W. De Young. 1992. Two roles for Ca^{2+} in agonist-stimulated Ca^{2+} oscillations. *Biophys. J.* 61:649–660.

Keizer, J., and L. Levine. 1996. Ryanodine receptor adaptation and Ca^{2+}-induced Ca^{2+} release-dependent Ca^{2+} oscillations. *Biophys. J.* 71: 3477–3487.

Khodakhah, K., and D. Ogden. 1993. Functional heterogeneity of calcium release by inositol trisphosphate in single Purkinje neurones, cultured cerebellar astrocytes, and peripheral tissues. *Proc. Natl. Acad. Sci. USA.* 90:4976–4980.

Klingauf, J., and E. Neher. 1997. Modeling buffered Ca^{2+} diffusion near the membrane: implications for secretion in neuroendocrine cells. *Biophys. J.* 72:674–690.

Kupferman, R., P. P. Mitra, P. C. Hohenberg, and S. S.-H. Wang. 1996. Analytical calculation of intracellular calcium wave characteristics. *Mol. Cell Biol.* 7:369a. (Abstr.).

Kupferman, R. P. P., P. C. Mitra, P. C. Hohenberg, and S. S.-H. Wang. 1997. Analytical calculation of calcium wave characteristics. *Biophys. J.* 72:2430–2444.

Li, W. H., J. Llopis, M. Whitney, G. Zlokarnik, and R. Y. Tsien. 1998. Cell-permeant caged InsP$_3$ ester shows that Ca^{2+} spike frequency can optimize gene expression. *Nature.* 392:936–941.

Li, Y. X., and J. Rinzel. 1994. Equations for InsP$_3$ receptor-mediated [Ca^{2+}]$_i$ oscillations derived from a detailed kinetic model: a Hodgkin–Huxley-like formalism. *J. Theor. Biol.* 166:461–473.

Luzzi, V., C. E. Sims, J. S. Soughayer, and N. L. Allbritton. 1998. The physiologic concentration of inositol 1,4,5-trisphosphate in the oocytes of *Xenopus laevis. J. Biol. Chem.* 273:28657–28662.

Lytton, J., M. Westlin, S. E. Burk, G. E. Shull, and D. H. MacLennan. 1992. Functional comparisons between isoforms of the sarcoplasmic or endoplasmic reticulum family of calcium pumps. *J. Biol. Chem.* 267: 14483–14489.

Mak, D. O. D., S. McBride, and J. K. Foskett. 1998. Inositol 1,4,5-tris-phosphate activation of inositol tris-phosphate receptor Ca^{2+} channel by ligand tuning of Ca^{2+} inhibition. *Proc. Natl. Acad. Sci. USA.* 95: 15821–15825.

Meldolesi, J., and T. Pozzan. 1998. The endoplasmic reticulum Ca^{2+} store: a view from the lumen. *Trends Biochem. Sci.* 23:10–14.

Miyawaki, A., J. Llopis, R. Heim, J. M. McCaffery, J. A. Adams, M. Ikura, and R. Y. Tsien. 1997. Fluorescent indicators for Ca^{2+} based on green fluorescent proteins and calmodulin [see comments]. *Nature.* 388: 882–887.

Monck, J. R., R. E. Williamson, I. Rogulja, S. J. Fluharty, and J. R. Williamson. 1990. Angiotensin II effects on the cytosolic free Ca^{2+} concentration in N1E-115 Neuroblastoma cells: kinetic properties of the Ca^{2+} transient measured in single fura-2 loaded cells. *J. Neurochem.* 54:278–287.

Patankar, S. V. 1980. Numerical Heat Transfer and Fluid Flow. Taylor and Francis, Washington, DC.

Press, W. H., S. A. Tuekolsky, W. T. Vetterling, and B. P. Flannery. 1992. Numerical Recipes in C (The Art of Scientific Computing). Cambridge University Press.

Roth, B., S. Yagodin, L. Holtzclaw, and J. T. Russell. 1995. A mathematical model of agonist-induced propagation of calcium waves in astrocytes. *Cell Calcium.* 17:53–64.

Schaff, J., C. C. Fink, B. Slepchenko, J. H. Carson, and L. M. Loew. 1997. A general computational framework for modeling cellular structure and function. *Biophys. J.* 73:1135–1146.

Schaff, J. C., B. M. Slepchenko, and L. M. Loew. 1999. Physiological modeling with the Virtual Cell framework. *In* Methods in Enzymology. M. Johnson, editor. Academic Press, San Diego. In press.

Slepchenko, B. M., J. C. Schaff, and Y. S. Choi. 2000. Numerical approach to fast reactions in reaction-diffusion systems: application to buffered calcium waves in bistable models. *J. Comput. Phys.* In press.

Sneyd, J., J. Keizer, and M. J. Sanderson. 1995. Mechanisms of calcium oscillations and waves: a quantitative analysis. *FASEB J.* 9:1463–1472.

Snider, R., and E. Richelson. 1984. Bradykinin receptor-mediated cyclic GMP formation in a nerve cell population (murine neuroblastoma clone N1E-115). *J. Neurochem.* 43:1749–1754.

Tang, Y., and H. G. Othmer. 1994. A model of calcium dynamics in cardiac myocytes based on the kinetics of ryanodine-sensitive calcium channels. *Biophys. J.* 67:2223–2235.

Terasaki, M., and L. A. Jaffe. 1991. Organization of the sea urchin egg endoplasmic reticulum and its reorganization at fertilization. *J. Cell Biol.* 114:929–940.

Ueda, T., S.-H. Chueh, M. Noel, and D. Gill. 1986. Influence of inositol 1,4,5-trisphosphate and guanine nucleotides on intracellular calcium release within the N1E-115 neuronal cell line. *J. Biol. Chem.* 261: 3184–3192.

Wagner, J., and J. Keizer. 1994. Effects of rapid buffers on Ca^{2+} diffusion and Ca^{2+} oscillations. *Biophys. J.* 67:447–456.

Wang, S. S.-H., A. A. Alousi, and S. H. Thompson. 1995. The lifetime of inositol 1,4,5-trisphosphate in single cells. *J. Gen. Physiol.* 105: 149–171.

Wang, S. S.-H., and S. H. Thompson. 1995. Local positive feedback by calcium in the propagation of intracellular calcium waves. *Biophys. J.* 69:1683–1697.

Xu, T., M. Naraghi, H. Kang, and E. Neher. 1997. Kinetic studies of Ca^{2+} binding and Ca^{2+} clearance in the cytosol of adrenal chromaffin cells. *Biophys. J.* 73:532–545.

Xu, X., W. ZEng, J. Diaz, and S. Muallem. 1996. Spacial compartmentalization of Ca^{2+} Signaling copmlexes in pancreatic acini. *J. Biol. Chem.* 271:24684–24690.